



HELSINKI UNIVERSITY OF TECHNOLOGY
Faculty of Information and Natural Sciences

Spin Effects in Circular Quantum Dots

Gustav Bårdsen

Master's thesis submitted in partial fulfillment of the requirements for the degree of Master of Science in Technology in the Degree Program in Engineering Physics.

Espoo, February 23rd 2008

Supervisor: Professor Risto Nieminen
Instructor: Docent Ari Harju

Author:	Gustav Bårdsen		
Degree Program:	Engineering Physics		
Major Subject:	Physics		
Minor Subject:	Computational Science and Engineering		
Title:	Spin effects in circular quantum dots		
Title in Finnish:	Spin-ilmiöitä sylinterisymmetrisissä kvanttipisteissä		
Chair:	Tfy-105 Theoretical and computational physics		
Supervisor:	Professor Risto Nieminen		
Instructor:	Docent Ari Harju		
<p>In semiconductor quantum dots, the motion of the electrons is restricted to a finite region of a two-dimensional semiconductor-semiconductor or semiconductor-insulator interface. Technologically, these systems provide interesting possibilities, for example, for future data processing applications where spin effects are utilized. Perhaps the most ambitious proposal is a spin-based quantum computer that utilizes tunable exchange interaction. Experimentalists have managed to get singlet–triplet transitions by tuning the confinement potential voltage in asymmetric quantum dots. Theoretically, some circularly symmetric quantum dots have a spin structure similar to the flux-penetrated ferromagnetic Heisenberg model, whereas other circular systems have a spin structure similar to the antiferromagnetic Heisenberg model.</p> <p>In this Master's Thesis, semiconductor quantum dots with different circularly symmetric confinement potentials were studied numerically in a wide range of magnetic field values. In addition to parabolic dots and rings, systems with other kinds of circularly symmetric confinement potentials were also studied. The emphasis of the study was on spin effects and differences between the systems. The studies were restricted to two-, four-, and six-electron systems. The calculations were done using the exact diagonalization (ED) and the variational quantum Monte Carlo (VMC) methods. The ED calculations were done with Landau-level mixing included, and the VMC calculations using single-configuration trial wave functions of the Slater-Jastrow type.</p> <p>The VMC method gave ground state energy values at most about two percent higher than the ED method, and mostly the agreement was considerably better. However, the VMC method failed almost completely to give the right spin ground states of the considered systems. In this study, for constant angular momenta it was found interesting spin oscillations as a function of the perturbation strength in the potential. These spin oscillations were explained using properties of the Laughlin and Halperin wave functions. There were also observed phase transitions between bands of ferromagnetic and antiferromagnetic regions, according to the Heisenberg model. A coupled dot-ring system had a clearly different spin structure than the dots and rings considered.</p>			
Number of pages:	74	Keywords:	quantum dot, spin, exact diagonalization, quantum Monte Carlo
Faculty fills			
Approved:		Library Code:	

Författare:	Gustav Bårdsen
Utbildningsprogram:	Utbildningsprogrammet för teknisk fysik
Huvudämne:	Fysik
Biämne:	Beräkningsbaserad vetenskap och teknik
Arbetets titel:	Spineffekter i cirkelsymmetriska kvantpunkter
Title:	Spin effects in circular quantum dots
Professur:	Tfy-105 Teoretisk och beräkningsfysik
Övervakare:	Professor Risto Nieminen
Handledare:	Docent Ari Harju
<p>I halvledarkvantpunkter är elektroner begränsade till ett ändligt område av en halvledar-halvledar- eller halvledar-isolator-gränsyta. Teknologiskt erbjuder dessa system intressanta möjligheter, till exempel för framtida spinbaserade tillämpningar inom databehandling. Den kanske mest ambitiösa tillämpningen är en spinbaserad kvantdator där bytesenergin mellan elektroner är reglerbar. Experimentellt har man lyckats åstadkomma singlet-triplet-transitioner genom att reglera begränsningspotentialen i asymmetriska kvantpunkter. Teoretiskt har en del cirkelsymmetriska kvantpunkter i ett yttre magnetfält en likadan spinstruktur som Heisenbergs ferromagnetiska modell, medan andra cirkelsymmetriska systems spinstruktur motsvarar Heisenbergs antiferromagnetiska modell.</p> <p>I detta diplomarbete har halvledarkvantpunkter med olika cirkelsymmetriska begränsningspotentialer, utsatta för ett yttre magnetfält, studerats numeriskt. Förutom paraboliska kvantpunkter och -ringar har också andra typer av cirkelsymmetriska system studerats. Huvudvikten i detta arbete har varit vid spineffekter och skillnader mellan de olika systemen. Studierna begränsades till system med två, fyra eller sex elektroner. Beräkningarna utfördes med exakt diagonalisering (ED) och kvant-Monte Carlo (QMC) -metoden. I ED-beräkningarna inkluderades alla förekommande Landau-nivåer, och QMC-beräkningarna gjordes enligt variationsprincipen med Slater-Jastrow-vågfunktioner med en enda konfiguration.</p> <p>QMC-metoden gav energivärden för grundtillståndet som var högst två procent högre än motsvarande ED-värden, och för det mesta var skillnaden betydligt mindre. QMC-metoden gav ändå för det mesta fel spingrundtillstånd. I denna studie upptäcktes vid konstanta rörelsemängdsmoment intressanta spinoscillationer som en funktion av förändringar i begränsningspotentialen. Dessa spinoscillationer kunde förklaras med hjälp av egenskaper hos Laughlins och Halperins vågfunktioner. Det observerades också fasövergångar mellan ferromagnetiska och antiferromagnetiska områden, enligt Heisenbergs modell. Ett kopplat kvantpunkt-ringsystem hade klart annorlunda spinstruktur än de kvantpunkter och -ringar som undersöktes.</p>	
Antalet sidor:	74 Nyckelbegrepp: kvantpunkt, spin, exakt diagonalisering, kvant-Monte Carlo
Fylls i av fakulteten	
Godkänt:	Bibliotekskod:

Acknowledgments

This Master's Thesis was done between July 2008 and February 2009 in the quantum many-body physics group in the Laboratory of Physics at Helsinki University of Technology. First of all, I want to thank my instructor Docent Ari Harju for suggesting the topic, for all his help, and for a generally positive attitude during these months. I also want to thank Professor Risto Nieminen for supervising the work. I am grateful to M. Sc. Eero Tölö for giving me the interaction matrix element code, some Monte Carlo code, and for useful advices, in particular concerning litterature. Likewise, I am grateful to Dr. Tech. Henri Saarikoski for valuable comments concerning the thesis. Many thanks to Janne Heikinheimo, Lauri Suoranta, and Kimmo Sääskilahti, with whom I shared office, and to M. Sc. Jani Särkkä. It has been a pleasure to work in the group, and particularly I remember the collective lunch breaks. I am also very grateful to all my friends and relatives, with whom I have been able to share more or less of my spare time.

Especially, I want to thank my parents who have always supported and encouraged me, during my double-degree studies in physics and music, and otherwise. My three brothers and the rest of our family are also very important to me. Finally, my warmest thanks belong to my dear Paula, who has enriched my life and given new dimensions to it.

Espoo, February 23rd 2009

Gustav Bårdsen

Contents

Acknowledgments	iv
1 Introduction	1
2 Physical background	4
2.1 Semiconductor quantum dots	4
2.2 Microscopic model	6
2.3 Single-electron system	7
2.3.1 Planar electrons and Landau levels	7
2.3.2 Wave functions	9
2.4 Many-electron system	11
2.4.1 Conservation of angular momentum	11
2.4.2 Energy level crossings	13
2.4.3 Effective Hamiltonian	14
2.5 Quantum Hall effects	15
2.5.1 The integer quantum Hall effect	18
2.5.2 The fractional quantum Hall effect	21
2.5.3 Laughlin's wave functions	21
2.5.4 Quantum Hall ferromagnetism	22
2.5.5 Quasiparticle excitations	23
3 Numerical methods	27
3.1 Single-electron states	27
3.2 The variational Monte Carlo method	28
3.2.1 The variational method	28
3.2.2 Monte Carlo integration	29
3.2.3 Importance sampling through Metropolis-walks	30
3.2.4 The VMC algorithm	31
3.2.5 Optimization of trial wave functions	32
3.2.6 Variational trial wave functions	33
3.2.7 Multi-configuration states	34

3.3	Exact diagonalization	36
4	Computational results	39
4.1	Confinement potentials	39
4.2	Single-electron systems	40
4.3	Few-electron droplets	41
4.3.1	Technical details of the calculations	41
4.3.2	VMC ground states	44
4.3.3	Spin structure	49
4.3.4	Spin oscillations	54
4.3.5	The coupled dot–ring system	61
5	Conclusions	64
A	Interaction matrix elements	75

Chapter 1

Introduction

During the last half of the 20th century, the charge of electrons has been utilized very successfully in digital logics. As the miniaturization of microelectronics continues, quantum effects become increasingly important. Simultaneously, the two last decades has seen an increasing scientific and technological interest in spin related phenomena, and in possible application of these in future data processing, communication and storage [1, 2, 3]. The currently existing data processing devices are entirely based on the classical binary bit, which can take one of two possible values. One of the most revolutionary ideas in spintronics is to use electron or nuclear spin as a qubit (quantum bit) in a hypothetical quantum computer [3, 4]. It has been shown that any quantum computer circuit can be implemented by tunable exchange interaction between spins [5]. Low-dimensional nanostructures, such as quantum dots, provide exciting possibilities as components in future data processing devices. A possible realization of the spin-based quantum computer utilizes tunable exchange interaction implemented in semiconductor quantum dots [5].

Technological needs and visions inspire also theoretical research in related fields. From a more theoretical point of view, the quantum Hall (QH) effects have shown a lot of interesting new phenomena in two-dimensional systems during the last two–three decades [6, 7, 8, 9], and a lot of questions are still open. In semiconductor quantum dots subjected to a strong magnetic field, the same kind of phenomena are observed as in quantum Hall systems in the thermodynamic limit [10, 11]. In particular, parabolically confined semiconductor quantum dots are often named quantum Hall droplets, as microscopic droplets of the incompressible quantum Hall liquid [12]. Concepts and findings related to the quantum Hall effects provide useful theoretical tools to analyse and understand the physics of semiconductor quantum dots.

The aim of the Thesis

The main objective of this Master's Thesis is to study numerically quantum dot systems with different circularly symmetric confinement potentials. Parabolically confined quantum dots and parabolic rings have been studied extensively. The circularly symmetric hard-wall quantum dot is also quite well known [10]. In addition to parabolic dots and rings, in this Thesis we will also investigate quantum dot systems with other kinds of circularly symmetric confinement potentials, such as a r^8 potential (proportional to r^8 , where r is the radius), parabolic and r^6 potentials with a Gaussian perturbation located at the center of the dot, and a coupled dot–ring system. In particular, we will study the transition and differences between such systems.

Inspired by the above mentioned possibility to implement a quantum computer that is entirely based on tunability of the exchange interaction between spins, both experimental and theoretical research [13, 14, 15, 16] has been done on quantum dots and rings where the electrostatic confinement was tunable. In these studies, they found singlet–triplet spin transitions as a function of the gate voltage. The previous studies were all done with asymmetric confinement potentials. For a circular hard-wall quantum dot a spin spectrum similar to the flux-penetrated ferromagnetic Heisenberg model has been found [17], whereas for a certain parabolic ring it has been found [18] a structure similar to the antiferromagnetic Heisenberg model. Because interesting spin phenomena were observed in the systems with tunable gate voltage, and there was observed the difference between the hard-wall (quasi-ring) and ring spin structures, to be able to study the same kind of phenomena, we will include spin degree of freedom in our simulations. For the same reason, the emphasis of this study will be on investigating spin effects.

Since many of the systems we are going to investigate have not been studied before, we start with few-electron systems restricted to at most six electrons. As numerical methods, we choose the exact diagonalization (ED) and variational quantum Monte Carlo (VMC) methods. Because of the strong correlations present in quantum dots, in particular at high magnetic fields, these non-perturbative methods are more accurate than density-functional theory (DFT) based methods. The ED and VMC methods are also easier to implement, and the computational cost is acceptable, when the number of electrons is so small. More arguments for the choice of methods are given in Subsecs. 4.3.2 and 4.3.3.

The subject of this Thesis is, in a very general context, motivated by the three facts stated in the beginning of this chapter: the development of spintronics, the vision of a future spin-based solid-state quantum computer, and the theoretical interest in studying quantum dots as microscopic quantum

Hall droplets. However, the immediate motivation of this study is mainly given by the spin related findings of Hancock *et al.* [17] and by the above mentioned experimental and theoretical studies on voltage-tunable quantum dots.

Chapter 2

Physical background

In this chapter, we give a short description of quantum dots and the microscopic model we have used in our calculations. We consider the physics of a single planar electron in a constant magnetic field, and derive the conservation of angular momentum in a many-electron circularly symmetric quantum dot. We also present the Landau–Zener model for energy level crossings, and describe an effective model Hamiltonian for a ringlike many-body system. When analysing the results of this Thesis in Ch. 4, we are able to utilize theoretical concepts related to the QH effects to understand the phenomena observed. In Sec. 2.5, we will therefore introduce some of the most fundamental physical aspects of the very interesting QH effects.

2.1 Semiconductor quantum dots

In many cases when the dimensionality of a system is reduced, properties of the material change profoundly. As an example, the electronic density of states as a function of energy is very different in one-, two- and three-dimensional systems [19]. In a semiconductor quantum dot, electrons, possibly only a few, are confined on a small island at an interface between two different semiconductors or between an insulator and a semiconductor. The quantum dot can be considered either as zero-dimensional, because of the restriction in all directions, as semi-two-dimensional or, if the electrons are restricted to a ring-shaped region, as a one-dimensional system. As will be seen later, the reduced dimensionality makes the physics of quantum dots considerably different from 3D condensed matter systems. We consider here the system in the zero temperature limit. Actual experiments are usually done in the mK regime.

Assume that the work function ϕ , i.e. the difference in energy between the

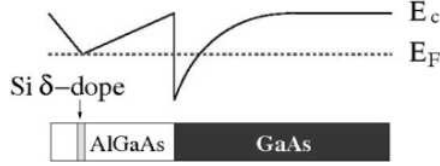


Figure 2.1: Schematic drawing of the band structure in a GaAs/ $\text{Al}_x\text{Ga}_{1-x}\text{As}$ heterojunction with a δ -doped donor layer that provides electrons. The conduction energy band is marked with E_c and the Fermi energy level with E_F . Electrons are trapped at the two-dimensional interface between GaAs and $\text{Al}_x\text{Ga}_{1-x}\text{As}$.

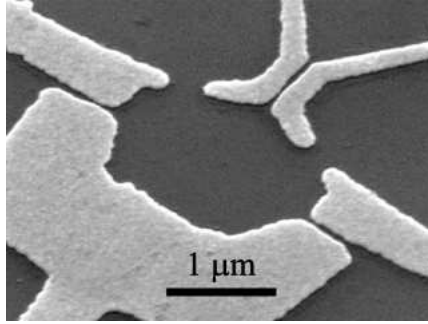


Figure 2.2: A lateral quantum dot with metallic gates restricting the electrons to a finite region of the two-dimensional trap. This figure is courtesy of the Nano-electronics group at the University of Basel [20].

Fermi level and the vacuum level, is larger in material A than in material B , thus $\phi_A > \phi_B$. To equalize the chemical potentials in the different materials, electrons flow from material B to A and accumulate at the planar interface. Because of the electron accumulation, the conduction band is bent near the interface (see Fig. 2.1). The thickness of the layer of trapped electrons at the interface is usually of the magnitude ~ 10 nm [6], which in semiconductors is typically smaller than the Fermi wavelength. As a result, the gap between the lowest and the second lowest energy level in the direction perpendicular to the interface is very large, and the electron system at the interface can be considered as purely two-dimensional.

In a semiconductor quantum dot, electrons are further restricted to a finite region of the two-dimensional interface. The electron gas can be trapped either by etching techniques or by electrostatic gates [10]. In Fig. 2.2 is given a picture of a lateral quantum dot where a voltage can be applied to the top

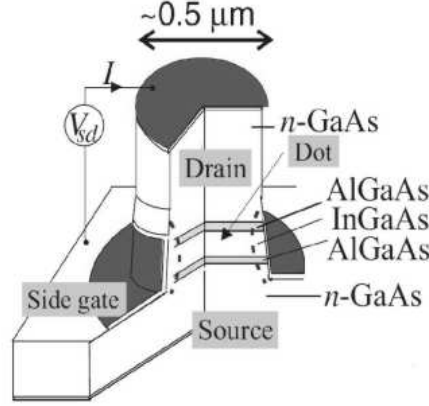


Figure 2.3: A schematic picture of a vertical quantum dot, as illustrated in Ref. [10]. The quantum dot is trapped in the InGaAs well.

gate electrodes (light grey color) to confine the electrons residing in a plane parallel to the top surface. By designing electrodes of different geometries and varying the gate voltages, the electrostatic potential can be changed and properties of the electron droplet can be tuned [16]. As seen from Fig. 2.2, the dimensions of the region of lateral confinement may be of the order of a few micrometers, whereas the layer thickness is only about ten nanometers. Alternatively, etching techniques can be used to make a pillar of semiconductor materials, as illustrated in Fig. 2.3. The diameter of such a vertical quantum dot is typically of the order of 10-100 nm [21]. The pillar can be surrounded by a metallic side gate, by which the electron island can be squeezed electrostatically.

2.2 Microscopic model

In this Masters's Thesis, we use an effective-mass approximation and model quantum dots as two-dimensional systems with the Hamiltonian

$$H = \sum_{i=1}^N \left(\frac{(-i\hbar\nabla_i + e\mathbf{A})^2}{2m^*} + V(r_i) \right) + \frac{e^2}{4\pi\epsilon} \sum_{i<j}^N \frac{1}{r_{ij}} + g^* \mu_B B S_z, \quad (2.1)$$

where N is the number of electrons, V is the external confinement potential, m^* is the effective electron mass, ϵ is the dielectric constant, g^* is the effective gyromagnetic ratio, μ_B is the Bohr magneton, and $S_z = \pm\frac{1}{2}$ stands for electron spin. The electrons are restricted to the Cartesian xy plane, and

the z axis is normal to the plane. r_{ij} is the distance between the electrons i and j and $\mathbf{B} = B\mathbf{e}_z$ is the magnetic field, where \mathbf{e}_z is the unit vector of the z axis. The magnetic vector potential \mathbf{A} is defined such that it gives the magnetic field \mathbf{B} by the relation

$$\mathbf{B} = \nabla \times \mathbf{A}. \quad (2.2)$$

Since we are interested in a quantum Hall system with disc geometry, we use the symmetric gauge, in which the vector potential is

$$\mathbf{A} = \frac{1}{2}B_z(y, -x, 0). \quad (2.3)$$

In all our calculations, we use the effective parameter values of GaAs, namely, $m^* = 0.067m_e$ and $\epsilon = 12.7$. To enhance the spin effects, we set $g^* = 0$, even if the normal value in GaAs is -0.44 . The effective gyromagnetic factor g^* , which in a semiconductor largely depends on spin-orbit coupling, can be altered by subjecting the system to hydrostatic pressure. In fact, experimentally, the gyromagnetic factor, and thereby also the Zeeman term, can be made vanishingly small [41]. The effective Zeeman gap can also be changed by using the tilted-field method [6, 34] or by using a suitable concentration of Al in $\text{Al}_x\text{Ga}_{1-x}\text{As}$ together with a low-voltage electrical bias [42]. From an experimental point of view it may thus be justified to set the gyromagnetic factor g^* to zero in a theoretical model. The effective mass m^* is determined by the periodic potential of the GaAs crystal.

2.3 Single-electron system

2.3.1 Planar electrons and Landau levels

We are next going to study a system of only one electron restricted to the xy plane, where a perpendicular magnetic field $\mathbf{B} = (0, 0, -B)$, $B \geq 0$, is applied. First, we assume there is no external confinement potential and the Zeeman term is neglected. The Hamiltonian is simply

$$H = \frac{1}{2m} [(p_x + eA_x)^2 + (p_y + eA_y)^2], \quad (2.4)$$

where $p_i = -i\hbar\partial_i$ and A_i are the components i of the kinetic momentum \mathbf{p} and the external magnetic potential \mathbf{A} , respectively.

For the following calculations, it turns out to be useful to use the complex number z defined as

$$z = \frac{1}{2\ell_B}(x + iy), \quad z^* = \frac{1}{2\ell_B}(x - iy), \quad (2.5)$$

with the derivatives

$$\frac{\partial}{\partial z} = \ell_B \left(\frac{\partial}{\partial x} - i \frac{\partial}{\partial y} \right), \quad \frac{\partial}{\partial z^*} = \ell_B \left(\frac{\partial}{\partial x} + i \frac{\partial}{\partial y} \right). \quad (2.6)$$

Here $\ell_B = \sqrt{\hbar/eB}$ is the magnetic length, the fundamental length scale of a QH system. Let us further introduce the two pairs of operators

$$a = -\frac{i}{\sqrt{2}} \left(z + \frac{\partial}{\partial z^*} \right), \quad a^\dagger = \frac{i}{\sqrt{2}} \left(z^* - \frac{\partial}{\partial z} \right) \quad (2.7)$$

and

$$b = \frac{1}{\sqrt{2}} \left(z^* + \frac{\partial}{\partial z} \right), \quad b^\dagger = \frac{1}{\sqrt{2}} \left(z - \frac{\partial}{\partial z^*} \right). \quad (2.8)$$

These operators obey the canonical Bose commutation relations

$$[a, a^\dagger] = [b, b^\dagger] = 1, \quad [a, b] = [a^\dagger, b] = 0. \quad (2.9)$$

Furthermore, the operators a^\dagger and b^\dagger are the Hermitian conjugates of a and b , respectively. These conditions are sufficient for the operators a^\dagger and b^\dagger to be bosonic creation operators, and a and b their respective annihilation operators.

The Hamiltonian (2.4) can be written [6] in terms of the operators (2.7) as

$$H = \left(a^\dagger a + \frac{1}{2} \right) \hbar \omega_c, \quad (2.10)$$

where $\omega_c = eB/m$ is the cyclotron frequency. Since a^\dagger and a are a creation-annihilation operator pair, it follows that $N = a^\dagger a$ is a number operator that counts the number of quanta described by the operator pair. Thus,

$$N|n\rangle = n|n\rangle, \quad (2.11)$$

where $|n\rangle$ is the eigenvector corresponding to n quanta. Consequently, the energy spectrum of the Hamiltonian (2.10) is

$$E_{n'} = (n' + \frac{1}{2}) \hbar \omega_c, \quad (2.12)$$

with $n' \in \{0, 1, 2, \dots\}$. The manifold of states with the same n' is called the n' th Landau level.

The angular momentum in the direction of the magnetic field can be written [6, 22]

$$L_z \equiv xp_y - yp_x = \hbar(b^\dagger b - a^\dagger a). \quad (2.13)$$

Using the commutation relations (2.9) of the creation and annihilation operators, we get $[L_z, H] = 0$. Thus, the z component of the angular momentum l_z is a good quantum number in a system with the Hamiltonian of Eq. 2.4.

2.3.2 Wave functions

From the commutation relations (2.9), one can see that the two operator pairs represent different kinds of bosonic quanta. Let the operator a^\dagger be related to the quantum number n' and the operator b^\dagger to the quantum number $l' \in \{0, 1, 2, \dots\}$. Then, the Fock vacuum $|0\rangle$ is defined as [6]

$$a|0\rangle = 0, \quad b|0\rangle = 0, \quad (2.14)$$

and the other Fock states can be constructed from the vacuum state as

$$|n', l'\rangle = \frac{1}{\sqrt{n'!l'!}} (a^\dagger)^{n'} (b^\dagger)^{l'} |0\rangle, \quad (2.15)$$

where the creation operators add n' and l' quanta, respectively, to the Fock vacuum state.

The condition of the ground state wave function $\psi_0(z, z^*)$ is, according to (2.14),

$$a\psi_0(z, z^*) = -\frac{i}{\sqrt{2}} \left(z + \frac{\partial}{\partial z^*} \right) \psi_0(z, z^*) = 0. \quad (2.16)$$

The resulting differential equation has the general solution

$$\psi_0(z, z^*) = f(z) \exp(-zz^*), \quad (2.17)$$

where $f(z)$ is an arbitrary analytic function. The condition (2.16) is in the case of a QH system called the lowest-Landau-level (LLL) condition.

Using the Fock vacuum condition (2.14) and the definitions of the operators b^\dagger and b in (2.8), the wave function corresponding to the LLL state $|0, l'\rangle$ can be found to be [6]

$$\psi^{l'}(z, z^*) = \langle \mathbf{x} | 0, l' \rangle = \sqrt{\frac{2^{l'}}{2\pi\ell_B^2 l'!}} z^{l'} e^{-|z|^2}. \quad (2.18)$$

Here $|\mathbf{x}\rangle$ denotes a position eigenvector. If the length is measured in units of $\lambda = \sqrt{\hbar/m\omega_c} = \sqrt{2}\ell_B$, then the wave function of the generic state (2.15) can be written [21, 23]

$$\psi_{n'}^l = \sqrt{\frac{2n!}{(n+|l|)!}} r^{|l|} e^{i\theta l} L_{n'}^{|l|}(r^2) \exp(-r^2/2), \quad (2.19)$$

where $r = \sqrt{x^2 + y^2}$, $\theta = \arctan(y/x)$, $l = l' - n'$ is the angular momentum quantum number, n' is the Landau level quantum number, and n is defined

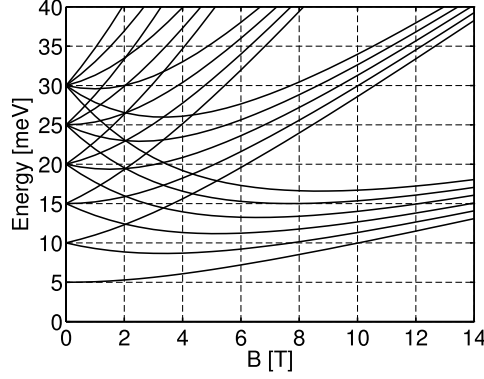


Figure 2.4: The Fock-Darwin energy spectrum as a function of the magnetic field in a system with 5 meV confinement strength.

through the relation $n' = (n - |l|)/2$. L is the associated Laguerre polynomial defined recursively as

$$L_0^l(x) = 1, \quad (2.20)$$

$$L_1^l = -x + l + 1 \quad (2.21)$$

and

$$(n+1)L_{n+1}^l(x) = (2n+l+1-x)L_n^l(x) - (n+l)L_{n-1}^l(x). \quad (2.22)$$

The energy as a function of the quantum numbers (n, l) ,

$$E_{n,l} = (n+1-l)\frac{\hbar\omega_c}{2}, \quad (2.23)$$

is obtained by substituting the expression of n' into Eq. (2.12).

Assume the electron is further restricted by a parabolic confinement potential

$$V(r) = \frac{1}{2}m^*\omega_0^2 r^2, \quad (2.24)$$

where ω_o determines the strength of the confinement. If the length measure is replaced by $\lambda = \sqrt{\hbar/m\omega}$, where $\omega = \sqrt{\omega_0^2 + \omega_c^2/4}$, then the system can be shown to have the same wave function (2.19) as obtained above and the single-particle energy is [23, 24]

$$E_{n,l} = \left(n+1 - \frac{\omega_c}{2\omega}l\right)\hbar\omega. \quad (2.25)$$

These so-called Fock-Darwin energy levels are illustrated in Fig. 2.4. In the high magnetic field limit we get

$$E_{n,l} = \left(n+1 - \frac{\omega_c}{2\omega}l\right)\hbar\omega \xrightarrow{\omega_c \rightarrow \infty} (n+1-l)\hbar\omega_c \propto (n+1-l)B, \quad (2.26)$$

and the different Landau levels can be seen in the energy spectrum as bands that are asymptotically linear functions of the magnetic field.

2.4 Many-electron system

2.4.1 Conservation of angular momentum

Let us write the many-body Hamiltonian of Eq. (2.1) in the more compact form

$$H = T + U_r + U_c + U_z, \quad (2.27)$$

where T is the kinetic energy operator part, U_r is the restriction potential part, U_c is the Coulomb energy part and U_z is the Zeeman term. In Subsec. 2.3.1, we stated that the *single-particle* Hamiltonian (2.4) commutes with the angular momentum operator L_z . To show that the *many-particle* Hamiltonian (2.27) commutes with the angular momentum operator, we need to show that L_z commutes also with the Hamiltonian terms U_r , U_c and U_z .

Let $f(r)$ be a general scalar function, ϕ a wave function and $L_z^{(i)}$ the angular momentum operator L_z of particle i . Then, the commutation relation between L_i and f may be written

$$\begin{aligned} [L_z^{(i)}, f(r)]\phi &= (L_z^{(i)}f - fL_z^{(i)})\phi \\ &= (x_i p_{y_i} - y_i p_{x_i})(f\phi) - f(x_i p_{y_i} - y_i p_{x_i})\phi \\ &= -i\hbar[x_i(\partial_{y_i}f)\phi + x_i f \partial_{y_i}\phi - y_i(\partial_{x_i}f)\phi - y_i f \partial_{x_i}\phi \\ &\quad - x_i f \partial_{y_i}\phi + y_i f \partial_{x_i}\phi] \\ &= -i\hbar[x_i(\partial_{y_i}f) - y_i(\partial_{x_i}f)]\phi. \end{aligned} \quad (2.28)$$

We start by looking at one term $V(r_i)$ of the restriction potential part U_r . It may be intuitively obvious for the reader that a circularly symmetric potential commutes with the angular momentum operator, but let us prove it explicitly. Using the chain rule of differentiation and the relation $r_i = \sqrt{x_i^2 + y_i^2}$, we get

$$\begin{aligned} \partial_{x_i} V(r_i) &= \frac{\partial V(r_i)}{\partial r_i} \frac{\partial r_i}{\partial x_i} \\ &= \frac{x_i}{r_i} \frac{\partial V(r_i)}{\partial r_i}, \end{aligned} \quad (2.29)$$

and similarly for $\partial_{y_i} V(r_i)$ by interchanging x_i with y_i . Substitution of the expressions of the form (2.29) into the commutation relation (2.28) gives $[L_z^{(i)}, V(r_i)] = 0$. Because the relation $[L_z^{(i)}, V(r_j)] = 0$, $i \neq j$, holds trivially,

we find that the total angular momentum operator $L_z = \sum_{i=1}^N L_z^{(i)}$ commutes with U_r .

Let us now turn to the central force two-particle potential $V_c(r_{ij}) \propto 1/r_{ij}$ of the U_c operator. The distance between particles i and j is

$$r_{ij} = |\mathbf{r}_i - \mathbf{r}_j| = ((x_i - x_j)^2 + (y_i - y_j)^2)^{1/2}. \quad (2.30)$$

By calculating the derivatives $\partial(1/r_{ij})/\partial x_i$ and $\partial(1/r_{ij})/\partial y_i$ and ditto for the particle j , one can easily show that

$$[L_z^{(i)} + L_z^{(j)}, V_c(r_{ij})]\varphi = 0. \quad (2.31)$$

Thus, also the Coulomb term U_c commutes with the total angular momentum L_z . The Zeeman term U_z commutes with the angular momentum, since $[L_z, S_z] = 0$. Correspondingly, we conclude that the many-particle Hamiltonian operator (2.27) commutes with the total angular momentum, i.e. $[L_z, H] = 0$.

Assume A is an arbitrary linear quantum mechanical operator, H is a Hamiltonian operator and ψ is a solution of the time dependent Schrödinger equation

$$H\psi = i\hbar \frac{\partial}{\partial t} \psi. \quad (2.32)$$

The expectation value corresponding to the operator A in the state ψ is defined by

$$\langle A \rangle = \int d^2x \psi^*(\mathbf{x}, t) A \psi(\mathbf{x}, t). \quad (2.33)$$

A short calculation using the complex conjugate of Eq. (2.32) gives the time derivative of the average value $\langle A \rangle$,

$$\frac{d}{dt} \langle A \rangle = \frac{i}{\hbar} \langle [H, A] \rangle + \left\langle \frac{\partial A}{\partial t} \right\rangle. \quad (2.34)$$

We have shown that $[L_z, H] = 0$, and the angular momentum operator has no explicit time dependence. Using Eq. (2.34), we get for the topologically restricted 2D many-electron system with a constant perpendicular magnetic field

$$\frac{d}{dt} \langle L_z \rangle = 0, \quad (2.35)$$

i.e. the average of the total angular momentum in the z direction is conserved. The eigenvalue equation of the operator L_z is

$$L_z |m\rangle = \hbar m |m\rangle, \quad (2.36)$$

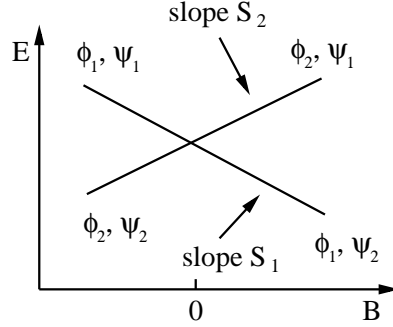


Figure 2.5: Two crossing energy levels 1 and 2 with slopes S_1 and S_2 , plotted as a function of the magnetic field B . The diabatic states $\phi_{1,2}$ are eigenstates corresponding to the energy levels 1 and 2, respectively. The adiabatic states $\psi_{1,2}$ are defined such that for $B \ll 0$, $\psi_1 = \phi_1$ and $\psi_2 = \phi_2$, while for $B \gg 0$, $\psi_1 = \phi_2$ and $\psi_2 = \phi_1$.

where m is an integer and $|m\rangle$ is the eigenstate corresponding to the quantum number m . The result of Eq. (2.35) implies that m is a good quantum number in a quantum dot system described by the Hamiltonian (2.1).

We have here shown that the total angular momentum is conserved in a circularly completely symmetric system. However, as will be seen from our many-electron calculations, different angular momentum states give the lowest energy for different magnetic fields. In order that the total angular momentum can change as a function of the magnetic field, there must thus be some impurities in the system that destroy the symmetry.

2.4.2 Energy level crossings

In this Thesis, we study quantum dots in different magnetic fields and with different electrostatic confinement potentials. The investigations are restricted to systems in equilibrium. However, since we are interested in tunable systems, it is motivated to mention a point considering the dynamics of such a system. As will be seen from our many-electron calculations, there are energy level crossings as a function of the magnetic field between states with different quantum numbers. We will here present the Landau-Zener model that describes the transition through an energy level crossing point, or alternatively an avoided level crossing.

Let us consider a system with two crossing energy levels 1 and 2, both with constant slopes S_1 and S_2 , as illustrated in Fig. 2.5. We name the eigenstates corresponding to the energy levels 1 and 2 as ϕ_1 and ϕ_2 , respectively. The

wave function of the system can be written as a linear combination of the diabatic states $\phi_{1,2}$,

$$\psi = A_1(t)\phi_1 + A_2(t)\phi_2, \quad (2.37)$$

where $A_1(t)$ and $A_2(t)$ are time dependent expansion coefficients. Let the system initially be in the state ϕ_2 , and let the magnetic field change with a constant velocity v . The probability that the system stays in the diabatic state ϕ_2 at magnetic fields above the crossing point (nonadiabatic transition) is given by the Landau–Zener formula [25]

$$P_{na} = \exp(-2\pi\omega_{12}\tau), \quad (2.38)$$

where $\omega_{12} \equiv |H_{12}|/\hbar$, $\tau \equiv |H_{12}|/v|S_{12}|$, $S_{12} = S_1 - S_2$, and H_{12} is the coupling matrix element in the diabatic basis. Here it is assumed that H_{12} is constant. The parameter ω_{12} is a characteristic frequency of the system, and τ describes the duration of the interaction. From Eq. (2.38), it is obvious that the probability that the system changes from the state ϕ_2 to ϕ_1 is large only if the transition is sufficiently slow. The limit of a slow transition, where the state at every moment is an eigenstate of the time-dependent Hamiltonian operator, is in quantum mechanics called an adiabatic transition [26]. In real systems, the slopes S_1 and S_2 , as well as H_{12} , are generally not constant. Despite this, the Landau–Zener model gives useful estimates of the dynamics in transition through energy level crossings [25, 27].

2.4.3 Effective Hamiltonian

When the electrons in a quantum ring or quasi-ring¹ become sufficiently localized, charge and spin excitations separate from each other [28]. This phenomenon is a non-perturbative effect due to the strong correlations in quantum dot systems at high magnetic fields. The resulting quasi-one-dimensional system can be described by the effective Hamiltonian

$$H = J \sum_{i,j} \mathbf{S}_i \cdot \mathbf{S}_j + \frac{1}{2I} L^2 + \sum_{\alpha} \hbar\omega_{\alpha} n_{\alpha}, \quad (2.39)$$

where the first term is an Heisenberg Hamiltonian that models the spin dynamics, the second term describes rigid rotation of the system, and the last term describes vibrational modes of the localized electrons. J is the nearest-neighbour coupling constant, I is the total moment of inertia, ω_{α} is the

¹By a quasi-ring we mean here a circularly symmetric system, where the most probable positions of all the electrons are located on the same one-dimensional ring.

Table 2.1: Angular momenta L and their corresponding spin values S for the ferromagnetic and antiferromagnetic Heisenberg models of a four-electron ring. Spin states corresponding to higher angular momenta are obtained by utilizing the periodicity of the spin sequence.

L		0	1	2	3
S	Ferr.	0	1	2	1
S	Antiferr.	1	1	0	1

vibration frequency, n_α is the number of excitation quanta of the vibrational mode, and L is the total angular momentum. In an antiferromagnetic system, $J > 0$, and in a ferromagnetic system, $J < 0$. This model Hamiltonian has been found to give the right total angular momentum–spin pairs of ground states and their lowest excitations for various quantum ring systems [18, 29, 30]. The total angular momentum–spin pairs according to the effective Hamiltonian (2.39) can be calculated using group-theoretical methods [18]. In Tab. 2.1 we have given the states of the ferromagnetic and antiferromagnetic systems. The spin sequence is N -periodic as a function of the angular momentum, where N is the number of electrons.

2.5 Quantum Hall effects

The quantum Hall effects are, along with for example superconductivity, among the most remarkable macroscopic quantum phenomena observed in condensed matter physics. By restricting electron systems to two dimensions at low temperatures and subjecting to a strong perpendicular magnetic field², a lot of new interesting physics has been found. The integer quantum Hall effect (IQHE) was discovered in 1980 by K. von Klitzing [31] and the fractional quantum Hall effect (FQHE) shortly thereafter, in 1982, by D. Tsui, H. Störmer and A. C. Gossard [32].

The classical equation of motion of an electron moving without dissipation in an xy plane with a magnetic field \mathbf{B} is

$$m\dot{\mathbf{v}} = -e(\mathbf{E} + \mathbf{v} \times \mathbf{B}), \quad (2.40)$$

where m is the electron mass, e is the elementary charge, \mathbf{E} the electric field,

²The conditions are [19] $\omega_c\tau \gg 1$ and $\hbar\omega_c \gg k_B T$, where $\omega_c \propto B$ is the cyclotron frequency, τ is the scattering relaxation time due to impurities in the material, k_B is the Boltzmann constant and T is the temperature of the system.

\mathbf{B} the magnetic field, and $\mathbf{v} = (v_x, v_y, 0)$ is the velocity. At equilibrium $\dot{\mathbf{v}} = 0$, and one gets the relation $\mathbf{E} = -\mathbf{v} \times \mathbf{B}$. Let $\mathbf{B} = (0, 0, -B)$, where $-B < 0$. The current density of a homogeneous electron gas with areal electron density ρ is $\mathbf{J} = -e\rho\mathbf{v}$. This can now be written as

$$\mathbf{J} = (J_x, J_y, J_z) = \frac{e\rho}{B}(E_y, -E_x, 0). \quad (2.41)$$

E. H. Hall discovered in 1879 that if the current is restricted to flow in the x direction, then there is induced an electric field E_y perpendicular to the direction of current flow, as seen from Eq. (2.41). This is the core of the classical Hall effect.

Assume that $J_y = 0$. Then, the Hall resistivity R_{xy} is by Eq. (2.41)

$$R_{xy} \equiv \frac{E_y}{J_x} = \frac{B}{e\rho} \quad (2.42)$$

and the diagonal resistivity

$$R_{xx} \equiv \frac{E_x}{J_x} = 0. \quad (2.43)$$

Classically, the Hall resistivity R_{xy} is thus expected to depend linearly on the applied magnetic field B . However, at temperatures close to the absolute zero point and in high magnetic fields, quantum effects become important and there is observed deviations from the linear behaviour of R_{xy} . As originally observed by Klitzing *et al.* [31], the IQHE can be seen [6] as plateaux in the Hall resistivity at values

$$R_{xy} = \frac{h}{\nu e^2}, \quad (2.44)$$

where ν is an integer and h is Planck's constant, and as dips in the diagonal resistivity R_{xx} (see Fig. 2.6). The FQHE was observed in the same way as plateaux in R_{xy} and dips in R_{xx} , but in this case ν was a fraction $\nu = n/m$, where n and m are integers (see Fig. 2.6). It is remarkable that the resistivity can be expressed only by the fundamental constants h and e , independent of impurities and geometric details of the macroscopic material. A surprising fact is also how accurate the quantization is: The accuracy of R_{xy} has been better than 10^{-7} , while resistivity values R_{xx} as low as $< 10^{-10} \Omega$ have been measured [34, 35].

By comparing Eqs. (2.42) and (2.44), one gets the relation

$$\nu = \frac{2\pi\hbar\rho}{eB} = 2\pi\ell_B^2\rho, \quad (2.45)$$

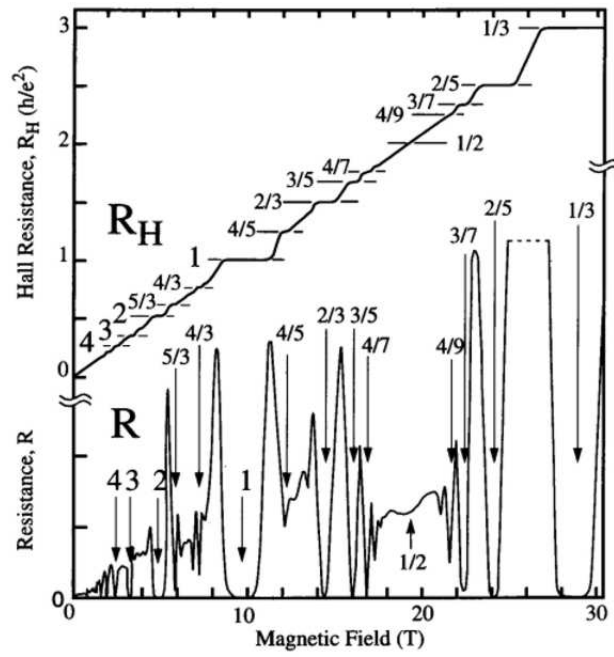


Figure 2.6: The IQHE and FQHE, as observed in the Hall resistivity $R_{xy} = R_H$ and the diagonal resistivity $R_{xx} = R$ of a 2D electron gas at a GaAs/AlGaAs interface [33]. The plateaux in R_H and dips in R corresponding to filling fractions ν are denoted by integers/fractions.

where $\ell_B = \sqrt{\hbar/eB}$ is the magnetic length. Since the number of states per area in a Landau level is $1/2\pi\ell_B^2$ [6], the parameter ν can be written as

$$\nu = \frac{N}{N_S}, \quad (2.46)$$

where N is the number of electrons and N_S the number of states on one Landau level. Because of this relation, the parameter ν is called the filling factor or, more precisely, the Landau-level filling factor. The filling factor can also be expressed as

$$\nu = N \frac{\Phi_D}{\Phi}, \quad (2.47)$$

where $\Phi_D \equiv h/e$ is the Dirac flux quantum and $\Phi = BA$ is the magnetic flux through the cross-section A of the 2D electron system.

2.5.1 The integer quantum Hall effect

Contrary to the FQHE, the IQHE can be understood in terms of an independent electron model. The integer Hall quantization can be explained in several different ways. An elegant explanation is the gauge invariance approach proposed by Laughlin [34, 36], which shows that the effect is due to gauge invariance and mobility gaps (energy regions where the diagonal conductivity $\sigma_{xx} = 0$). We will here give a derivation following Ezawa [6]. This presentation is a bit lengthier than the gauge invariance approach, but it is perhaps more transparent, since few and simple physical assumptions are needed.

In the following calculations, the *Landau gauge*, with the vector potential

$$\mathbf{A} = B(y, 0, 0), \quad (2.48)$$

is the most convenient. The magnetic field $B_z = -B$. When an electric field E is applied in the y direction, the Hamiltonian becomes

$$H = \frac{1}{2m} [(p_x + eBz)^2 + p_y^2] + eyE. \quad (2.49)$$

The eigenvalue problem of this Hamiltonian is exactly solvable, and according to Ezawa [6] it gives the wave functions

$$\psi_k(x, y) = \frac{1}{\sqrt{\pi^{1/2}\ell_B}} \exp(ikx) \exp \left[-\frac{1}{2\ell^2(y - \bar{y})^2} \right] \quad (2.50)$$

and the energy eigenvalues

$$E(k) = -eE\ell_B^2 k - \frac{(eE\ell_B)^2}{2\hbar\omega_c}. \quad (2.51)$$

In the wave function expression, we used the definition

$$\bar{y} \equiv -k\ell_B^2 - \frac{eE}{\hbar\omega_c}\ell_B^2. \quad (2.52)$$

The quantum field (annihilation) operator is generally defined as

$$\Psi \equiv \int \frac{d\mathbf{k}}{\sqrt{2\pi}} c(k) \psi_k(x, y), \quad (2.53)$$

where $c(k)$ is the annihilation operator of the state $|k\rangle$, corresponding to $\psi_k(x, y) = \langle \mathbf{x} | k \rangle$. By substituting the wave function (2.50) into (2.53), the operator may be written as

$$\Psi = \frac{1}{\sqrt{\pi^{1/2}\ell_B}} \int \frac{d\mathbf{k}}{\sqrt{2\pi}} c(k) \exp(ikx) \exp\left[-\frac{1}{2\ell^2(y-\bar{y})^2}\right]. \quad (2.54)$$

In the considered quantum field theory formulation, the electric current is calculated as the Nöther current

$$J_\mu = -\frac{ie\hbar}{2m} [\Psi^\dagger (D_\mu \Psi) - (D_\mu \Psi)^\dagger \Psi], \quad (2.55)$$

where

$$D_\mu \equiv \partial_\mu + i\frac{e}{\hbar} A_\mu, \quad (2.56)$$

and $\mu \in \{x, y, z\}$. Combining Eqs. (2.54) and (2.55), and utilizing the commutation relations

$$\{c(n), c(m)\} = \delta_{nm} \quad (2.57)$$

and

$$\{\Psi(\mathbf{x}), \Psi(\mathbf{y})\} = \delta(\mathbf{x} - \mathbf{y}), \quad (2.58)$$

we get

$$J_x(x, y) = -\frac{e\hbar}{2m} \partial_y \rho(x, y) + \frac{e^2 \ell_B^2}{\hbar} E \rho(x, y) \quad (2.59)$$

and

$$J_y(x, y) = \frac{e\hbar}{2m} \partial_x \rho(x, y) \quad (2.60)$$

as current operators. In an infinite 2D IQHE system the density is homogeneous, $\rho(x, y) = \nu/(2\pi\ell_B^2)$ at an integer filling fraction ν , and we obtain the current density expressions

$$J_x = \nu \frac{e^2}{2\pi\hbar} E, \quad J_y = 0. \quad (2.61)$$

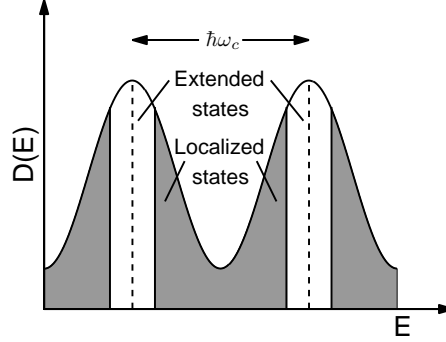


Figure 2.7: Density of states (DOS) as a function of energy of a 2D electron gas in a magnetic field. In pure samples the DOS consists of delta peaks, here denoted by the dashed vertical lines. In the presence of disorder, the peaks are broadened and there are found mobility edges between extended and localized states.

The corresponding resistivities

$$R_{xy} = \frac{E_y}{J_x} = \frac{h}{\nu e^2}, \quad R_{xx} = \frac{E_x}{J_x} = 0 \quad (2.62)$$

are the same as the measured IQHE resistivities presented in the previous section.

The derivation above suggests that the Hall conductivity is quantized, but it does not explain the magnetic field ranges of the Hall plateaux, for which $R_{xx} = 0$ (see Fig. 2.6). Ezawa [6] explains the formation of plateaux in the following way: When the external magnetic field is altered in the vicinity of the point of a given integer or fractional filling factor, the added or removed magnetic flux quanta are used to create quasiparticles (more about quasiparticle excitations in Subsec. 2.5.5). These quasiparticles are charged objects, and become therefore localized by impurities and do not contribute to the current at zero temperature. The resistivity stays therefore constant in a narrow range around the exact filling fractions. When the magnetic field is changed more, there are created more quasiparticles, and at a certain point there will be too many quasiparticles to be localized by the impurities of the material sample. As a consequence, the resistivity must change and the QH state is destroyed. Laughlin [36] and Prange [8] explain the formation of the resistivity plateaux by the broadening of the density of states peaks of a pure QH system due to impurities in the material (see Fig. 2.7). The Fermi level changes as a function of the magnetic field. The

longitudinal resistivity is zero in the regions of localized states, and in those intervals the Hall resistivity is therefore kept constant.

2.5.2 The fractional quantum Hall effect

When deriving the quantization of the Hall resistivity in the previous section, we assumed the density to be homogeneous. This assumption is fulfilled in the IQHE case without taking into account interactions between the particles, because each Landau level is either completely filled or empty. In the $\nu = 1/m$ case, where $m > 1$ is an odd integer, only $1/m$ of the states of the lowest Landau level are occupied. Consequently, without considering interaction effects, the system is vastly degenerate and may be inhomogeneous. Because experimentally the system shows similar resistivity plateaux at $\nu = 1/m$ as when ν is an integer, one is led to the assumption that the system must be homogeneous and incompressible also when $\nu = 1/m$. The fractional Hall plateaux are observable only in samples of high mobility, and impurities are thus not expected to be important for the FQHE [34]. The only interaction present in the system is the Coulomb force, and it must therefore be responsible for the incompressibility. Thus, while the IQHE can be described entirely using single-electron states, the FQHE is a result of many-body interactions. As stated by Laughlin [12], because of the interactions, the 2D electrons condense into a new collective state of matter. Jain [37] proposed a so-called composite-fermion approach: In a $\nu = 1/m$ state, each electron is assumed to be bound to $2p$ ($p \geq 1$ is an integer) magnetic flux quanta. The composite-fermions make up an integer QH state. This is one way to explain the FQHE. Alternatively, if $(2p+1)$ flux quanta are bound to each electron, we get composite bosons [6]. Since the composite particles are bosons, they condense into an incompressible state.

2.5.3 Laughlin's wave functions

R. B. Laughlin has with his theoretical work to a significant extent contributed to the present understanding of the FQHE. Based on studies of few-particle quantum Hall systems, he proposed [9, 12] for the $\nu = 1/m$ ground state the Jastrow-type³ [38] N -electron (spin polarized) wave function

$$\Psi_{Lm} = \prod_{i < j}^N (z_i - z_j)^m e^{-\sum_{i=1}^N |z_i|^2}, \quad (2.63)$$

³See Subsec. 3.2.6 for an example of how a Jastrow function can be used in the variational method.

where $z = x - iy$, and m is assumed to be odd. We have here neglected the normalization constant. This wave function is antisymmetric with respect to interchange of positions of two electrons when m is odd, and satisfies thus the Pauli exclusion principle. By comparing the wave function (2.63) with the LLL single-electron states of Eq. (2.18), one can see that the Laughlin wave function is comprised solely of LLL single-electron states. The angular momentum of a single-electron state ψ'' (Eq. (2.18)) is l' ($\hbar = 1$), and the total angular momentum is obtained by summing up single-electron angular momenta. Consequently, one finds that the total angular momentum of Ψ_{Lm} , $L = (N - 1)Nm/2$, is conserved. When searching for a variational wave function with a Jastrow factor, Laughlin found [9] that the function (2.63) is completely determined and leaves no variational degrees of freedom left. The N -body state Ψ_{L1} has total angular momentum $L = (N - 1)N/2 = \sum_{i=1}^N i$, and consists of the single-electron angular momentum states $\{l_i\} = \{0, 1, 2, \dots, N - 1\}$. This is the lowest possible angular momentum state of a spin polarized system compatible with fermion antisymmetry, and is therefore called the maximum-density droplet (MDD) [39]. Laughlin also showed generally that the state described by Ψ_{Lm} is an incompressible liquid [12].

2.5.4 Quantum Hall ferromagnetism

In a single-electron system with a vanishingly small gyromagnetic factor, each Landau level contains two levels almost equal in energy. In a many-body system, this degeneracy is broken due to exchange interaction and Coulomb energy (see Fig. 2.8). As a result, the spins of the system are polarized in a direction determined by the small Zeeman term. In a QH system in the thermodynamical limit, the field-theoretical Hamiltonian of the exchange interaction can be written [6]

$$H_{ex} = 2J \sum_i \int d^2x [\partial_k \mathbf{S}_i(\mathbf{x})]^2, \quad (2.64)$$

where $\mathbf{S}_i(\mathbf{x})$ is the spin field and $J = E_C^0/16\sqrt{2\pi}$ is the spin stiffness. Here $E_C^0 = e^2/4\pi\epsilon\ell_B$ is the Coulomb energy associated with the magnetic length ℓ_B . The Hamiltonian of Eq. 2.64 is a so-called nonlinear sigma model [40]. Since $J > 0$, the exchange energy is minimized when the derivatives of the spin field vanish everywhere, i.e. when the spin direction is constant throughout the system. Intuitively, one can think that the Coulomb energy is smaller between electrons of equal spin, because the average interparticle distance becomes larger due to the exchange hole. The energy gap between the spin

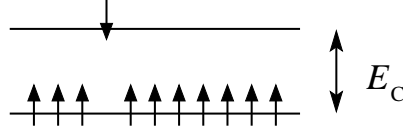


Figure 2.8: Even in the limit of vanishing Zeeman energy, there is a finite energy gap E_C between the different spin energy levels. The splitting of the energy levels is, as in ferromagnets, an exchange interaction effect.

levels makes the system incompressible at $\nu = 1$. In the same way, according to the composite-particle theory, the $\nu = 1/m$ (m odd) states are also incompressible. A macroscopic QH system that can be described by the Hamiltonian (2.64) is called a QH ferromagnet.

At sufficiently high magnetic fields, the Zeeman gap, $\Delta_Z = |g^* \mu_B B|$, becomes larger than the typical Coulomb energy, $E_C^0 = e^2/4\pi\epsilon\ell_B$, and the spin degree of freedom is frozen. However, in a typical semiconductor at 10 Tesla, the ratio $\tilde{r} \equiv \Delta_Z/E_C^0$ is only about 0.02 [6]. As stated in Sec. 2.2, in experiments it is even possible to tune the gyromagnetic factor g^* to zero. Consequently, spin effects may be expected in QH systems.

2.5.5 Quasiparticle excitations

The elementary excitations of a stable $\nu = 1/m$ Laughlin state are quasiparticles and quasiholes with charge $\pm e/m$. The fractionally charged quasiparticle and quasihole excitations are, like the spin-charge separation mentioned in Subsec. 2.4.3, examples of non-perturbative effects due to the strong correlations in a fractional QH system. The excitation is gapful, which means that a finite creation energy $\Delta_{qp} + \Delta_{qh}$ is needed to create a quasiparticle-quasihole pair from the ground state. The quasiparticles (quasiholes) are antivortices (vortices) in a spin-polarized system, while they are antiskyrmions (skyrmions) in a QH ferromagnet (a QH system with spin degree of freedom) [6].

Let us first consider the spin-polarized case. We use a thought experiment to verify that an elementary excitation is created, when adding a magnetic flux quantum to a QH system. By heuristic arguments, we show that the excitation is a vortex or an antivortex.

Assume an infinitely thin magnetic solenoid is inserted perpendicularly at the origin of a QH system (see Fig. 2.9). We increase the magnetic flux through the solenoid adiabatically (slowly) from zero to $n\Phi_0$, where Φ_0 is the Dirac flux quantum and n is an integer. Since the change is made

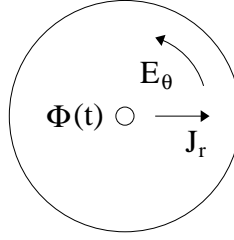


Figure 2.9: Formation of a vortex as an elementary excitation. An infinitely thin magnetic solenoid crosses the 2D surface perpendicularly at the origin. The time-dependent flux $\Phi(t)$ through the solenoid induces an electric field E_θ , which in turn generates a Hall current J_r , perpendicular to E_θ .

adiabatically, the system remains all the time an eigenstate of the changing Hamiltonian. Due to the Aharonov–Bohm effect⁴, the wave function in a system pierced by a magnetic flux Φ is transformed as

$$\psi(x, y) \rightarrow \exp\left(\frac{i\theta(x, y)e}{h}\Phi\right)\psi(x, y), \quad (2.65)$$

where $\psi(x, y)$ is the initial wave function, and $\theta(x, y) = \arctan(y/x)$. At the maximum flux value, the wave function is

$$\psi'(x, y) = \exp(i\theta(x, y)n)\psi(x, y). \quad (2.66)$$

This change can be removed by a singular gauge transformation. Thus, the final Hamiltonian is the same as the initial one. Because the ground state is non-degenerate, we conclude that the state pierced by a $n\Phi_0$ flux must be an excitation of the ground state.

According to Faraday’s induction law, a time-dependent magnetic flux induces an electric field

$$E_\theta = \frac{1}{2\pi r} \frac{d\Phi}{dt}, \quad (2.67)$$

directed in the plane, around the solenoid (see Fig. 2.9). The electric field, in turn, generates the radially directed Hall current

$$J_r = \frac{e\rho}{B}E_\theta, \quad (2.68)$$

as given by Eq. (2.42). This statement holds only sufficiently far from the solenoid. We can now calculate the charge of the created quasiparticles or

⁴The reader may consult any standard quantum mechanics textbook, for example [43], for an explanation of the Aharonov–Bohm effect.

quasiholes as

$$q = 2\pi r \int dt J_r = \frac{e\rho}{B} \int dt \frac{d\Phi}{dt} = \frac{ne\rho}{B} \Phi_0 = n\nu e. \quad (2.69)$$

We notice that the charge of a single quasihole/quasielectron ($n = 1$) is $\pm e/m$ at the filling fraction $\nu = 1/m$. Since the charge $-|n|\nu e$ is either added to or removed from the region around the solenoid, the excitations of the rotating electron system can be identified as vortices or antivortices.

When a flux $\pm\Phi_0$ is added, according to Eq. (2.65) the polynomial part of the wave function is transformed as $z^l \rightarrow e^{\pm i\theta} z^l = z^{l+1} r^{\mp 1}$, where $r = |z|$. To get excitations that stay in the lowest Landau level, Laughlin suggested the transformations

$$z^l \rightarrow z^{l+1}, \quad z^l \rightarrow \frac{\partial}{\partial z} z^l \quad (2.70)$$

for creating vortices and antivortices, respectively. The Laughlin wave function for a $\nu = 1/m$ state with n_0 vortices added at the position (x_0, y_0) , i.e. the quasi-hole wave function, is

$$\begin{aligned} \Psi_{Lm}^{(-n_0)} &= \prod_i (z_i - z_0)^{n_0} \Psi_{Lm} \\ &= \prod_i (z_i - z_0)^{n_0} \prod_{i < j}^N (z_i - z_j)^m e^{-\sum_{i=1}^N |z_i|^2}, \end{aligned} \quad (2.71)$$

where $z_0 = x_0 - iy_0$. Unfortunately, the corresponding quasi-electron Laughlin wave function gives a wrong filling factor and inaccurate energies [44]. This wave function is therefore normally not used. Instead, other proposals for the quasi-electron trial wave function has been given, such as the wave function by Jain [45] and others [44, 46]. Halperin proposed [34, 47, 48] for a spin-unpolarized ($S = 0$) or partially polarized FQHE state the Laughlin-like wave function

$$\Psi_{Hm,n} = \prod_{i,\alpha} (z_i - z_\alpha)^l \prod_{i < j} (z_i - z_j)^k \prod_{\alpha < \beta} (z_\alpha - z_\beta)^{k'} \prod_j e^{-|z_j|^2} \prod_\alpha e^{-|z_\alpha|^2}, \quad (2.72)$$

where Roman and Greek letters are used for the two different spin states. The total filling factor of this state is [47]

$$\nu = \frac{k + k' + 2l}{kk' - l^2}. \quad (2.73)$$

It must be pointed out that the total spin of the Halperin two-component wave function is ill-defined for certain filling fractions; for example the state

$\nu = 2/3$ cannot be described by this wave function [28, 47]. The Halperin wave function is antisymmetric if, and only if, k and k' are odd integers and l is a positive integer.

In a QH ferromagnet, described by the effective Hamiltonian (2.64), charged quasiparticle excitations are skyrmions [6]. A skyrmion is a spin texture, where spins are rotated coherently to lower the Coulomb energy. Skyrmions may be considered as topological solitons⁵ spread over two energy levels. A skyrmion is reduced to a vortex when the radius of the excitation approaches zero [6], or in the limit when the Zeeman energy becomes strong. Interpretation of an excitation as a skyrmion is less clear for few-electron systems than for systems with a large number of particles [49].

⁵The interested reader may find some basic theory about topological solitons for example in Ref. [6].

Chapter 3

Numerical methods

In this Thesis we have used two different numerical methods for solving the time-independent many-body Schrödinger equation: The variational Monte Carlo (VMC) and the exact diagonalization (ED) method. In the first section of this chapter, we tell how the single-electron states were calculated for systems with non-parabolic confinement potentials. In Sec. 3.2, we explain the VMC method and also consider the many-body problem. In Sec. 3.3, the ED method is presented.

3.1 Single-electron states

The Fock-Darwin single-electron state of a quantum dot in a harmonic confinement potential was given in Eq. (2.19), i.e.

$$\psi_{n'}^l = \sqrt{\frac{2n!}{(n+|l|)!}} r^{|l|} e^{i\theta l} L_{n'}^{|l|}(r^2) \exp(-r^2/2). \quad (3.1)$$

For more general, non-parabolic electrostatic potentials we calculated the corresponding single-particle wave functions $\phi_{n'}^l$ as finite linear combinations of the harmonic oscillator states,

$$\phi_{n'}^l = \sum_{i=0}^M c_i \psi_i^l, \quad (3.2)$$

where c_i are real coefficients. The coefficients c_i were calculated by solving the Hamiltonian matrix equation

$$\mathbf{H}\mathbf{c} = E\mathbf{c}, \quad (3.3)$$

where $\mathbf{c} = (c_0, c_1, \dots, c_N)$, E is the energy, and \mathbf{H} is the Hamiltonian matrix. The Hamiltonian of a non-parabolic system can be written as

$$\hat{H} = \hat{H}_0 + V(r) - V_0(r), \quad (3.4)$$

where \hat{H}_0 is the single-electron Hamiltonian of a parabolic quantum dot, $V_0(r)$ is the confinement potential of \hat{H}_0 , and $V(r)$ is the confinement potential of the non-parabolic system. The matrix elements of \mathbf{H} can then be written

$$\begin{aligned} H_{ij} &= \langle \psi_i^l | \hat{H} | \psi_j^l \rangle \\ &= \langle \psi_i^l | \hat{H}_0 | \psi_j^l \rangle + \langle \psi_i^l | V(r) - V_0(r) | \psi_j^l \rangle. \end{aligned} \quad (3.5)$$

The first term of the right-hand side of Eq. (3.5) is known analytically; it is the Fock-Darwin energy given in Eq. (2.25). The integral $\langle \psi_i^l | V(r) - V_0(r) | \psi_j^l \rangle$ can be considered as a small perturbation when the potential $V(r)$ is close to a parabolic one.

3.2 The variational Monte Carlo method

3.2.1 The variational method

According to the variational principle, the ground state energy of a quantum system, E_0 , is the minimum value of the functional $E[\Psi]$, i.e.

$$E_0 \leq E[\Psi] \equiv \frac{\langle \Psi | H | \Psi \rangle}{\langle \Psi | \Psi \rangle}, \quad (3.6)$$

where H is the Hamiltonian operator and the domain of the vector $|\Psi\rangle$ is the full Hilbert space. The variational method, also called Ritz variational principle, gives an upper bound of the ground state energy. The algorithm consists of the following steps:

1. Choose a trial many-particle wave function $\Psi_\alpha(R)$ with variational parameters $\alpha = (\alpha_1, \dots, \alpha_N)$. R is a vector of the position coordinates of all the particles.
2. Calculate $E[\Psi_\alpha]$ according to Eq. (3.6).
3. If the stopping criterion for minimum energy is not fulfilled, get a new set of the parameters α from a minimization algorithm and return to step 2.

The VMC method [50] is a special case of the variational method where the integrals $E[\Psi_\alpha]$ are evaluated using a Metropolis Monte Carlo technique. In Subsecs. 3.2.2–3.2.4 we describe the Metropolis Monte Carlo integration method, and in Subsec. 3.2.5 we present the method used for optimization of the energy.

3.2.2 Monte Carlo integration

Suppose the task is to evaluate an integral I of a smooth function f on the interval $[a, b] \in \mathbb{R}$,

$$I = \int_a^b dx f(x). \quad (3.7)$$

Most standard numerical integration methods can be written into the form

$$I = \frac{(b-a)}{N} \sum_{i=1}^N w_i f(x_i), \quad (3.8)$$

where N is the number of grid points x_i and the weights w_i are constants determined by the method, independent of f .

For the given one-dimensional case, with equal separation h between subsequent grid points, the error estimate is $\sigma \sim h^k \sim N^{-k}$, where k is a positive integer. When integrating over a d -dimensional hypercube with side L , the total number of grid points becomes $N = (L/h)^d$. Consequently, $h \sim N^{-1/d}$ and the error scales as $N^{-k/d}$.

In Monte Carlo integration, the weights w_i are all 1 and the grid points x_i are chosen randomly, according to a given distribution. Assuming that the points x_i are independent and the distribution function is fixed, the terms $y_i = f(x_i)$ are also independent with a fixed distribution function. The central limit theorem¹ [51] then states for the standard deviation of the Monte Carlo integral, independently of the number of dimensions, $\sigma \sim N^{-1/2}$.

As seen from the error estimates, at low dimensions the polynomial based conventional methods with equally spaced grid points are to prefer. However, as the number of dimensions increases the Monte Carlo method becomes superior. For example, the Hamiltonian matrix element integrals of an N -body quantum system, as in Eq. (3.6), are of the dimension $d \times N$, where d is the space dimension of the system and N is the number of particles.

¹Let X_1, \dots, X_n be independent, identically distributed random variables with the same expectation value $E[X_i] = \mu$ and variance $Var[X_i] = \sigma^2 < \infty$, $i = 1, 2, \dots$. Then the classical central limit theorem states that the sum $X_1 + \dots + X_n$ approaches the normal distribution with mean $n\mu$ and variance $n\sigma^2$ as n goes towards infinity.

The k value of Simpson's rule is 4. Thus, depending on the prefactors, for two-dimensional systems with more than around 4 particles the Monte Carlo integration method converges faster than the Simpson's algorithm.

3.2.3 Importance sampling through Metropolis-walks

In practical calculations, the values of the integrand $f(x)$ can change a lot between different regions of the domain of x . To ensure that the sampling points are used efficiently in the integration, the random points can be taken from a distribution $\rho(x)$ with more or less the same shape as f . The integral can be written

$$\int_a^b dx f(x) = \int_a^b dx \rho(x) \left[\frac{f(x)}{\rho(x)} \right] \approx \frac{1}{M} \sum_{i=1}^M \frac{f(x_i)}{\rho(x_i)}, \quad (3.9)$$

where M is the number of sample points x_i taken from the distribution $\rho(x)$. This technique is called importance sampling.

A set of configurations $\mathcal{S} = \{x_i\}_i$ following the distribution $\rho(x)$ can be obtained using the Metropolis method [50, 52]. In the Metropolis method, the set \mathcal{S} is chosen through a Markov chain random walk. The Markov property, which defines Markov chains, is

$$P(x_{i+1}|x_i, x_{i-1}, \dots, x_0) = P(x_{i+1}|x_i), \quad (3.10)$$

where $P(x_{i+1}|x_i)$ is the probability to get x_{i+1} at step $i+1$ given the previous state x_i . Let $T(x \rightarrow x')$ be the probability of transition from state x to x' . Then, the equilibrium condition

$$T(x \rightarrow x')\rho(x) = T(x' \rightarrow x)\rho(x'), \quad (3.11)$$

the so-called detailed balance condition, can be shown to give a solution for T according to the stationary distribution $\rho(x)$. Further, let $t_{xx'}$ be the trial step probability and $a_{xx'}$ the acceptance probability in the transition from x to x' , so that $T(x \rightarrow x') = t_{xx'}a_{xx'}$. In the Metropolis method, we assume that $t_{xx'} = t_{x'x}$. Then, the detailed balance condition (3.11) gives

$$\frac{a_{xx'}}{a_{x'x}} = \frac{\rho(x')}{\rho(x)}. \quad (3.12)$$

The acceptance probability matrix elements $a_{xx'}$ are chosen following the rule

$$a_{xx'} = \begin{cases} \rho(x')/\rho(x), & \text{if } \rho(x') < \rho(x), \\ 1, & \text{if } \rho(x') \geq \rho(x). \end{cases} \quad (3.13)$$

This definition of $a_{xx'}$ satisfies Eq. (3.12). Accordingly, the set $\mathcal{S} = \{x_i\}$ obtained through a Metropolis walk will have the stationary distribution $\rho(x)$.

3.2.4 The VMC algorithm

In the VMC method [50], the energy expectation value $\langle E \rangle = E[\Psi_\alpha]$, determined by Eq. (3.6), has to be evaluated. The local energy of a system is defined as

$$E_L(R) = \frac{H\Psi_\alpha(R)}{\Psi_\alpha(R)}, \quad (3.14)$$

where H is the Hamiltonian operator and Ψ_α is a trial wave function. If Ψ_α is the exact eigenfunction of H , then $E_L(R)$ is a constant with respect to R . The variations of $E_L(R)$ as a function of the coordinates R vanish as Ψ_α approaches the exact wave function. Thus, if the trial wave function is reasonably close to the exact eigenvector, one can assume $E_L(R)$ to be a good integrand in the importance sampling method. The integration formula becomes

$$\langle E \rangle = \frac{\int dR \Psi_\alpha^*(R) \Psi_\alpha(R) E_L(R)}{\int dR \Psi_\alpha^*(R) \Psi_\alpha(R)}. \quad (3.15)$$

Comparing with the case of a general Metropolis random walk, the stationary distribution is here

$$\rho(R) = \frac{\Psi_\alpha^*(R) \Psi_\alpha(R)}{\int dR \Psi_\alpha^*(R) \Psi_\alpha(R)}. \quad (3.16)$$

The resulting algorithm of the VMC method is the following:

```

Give randomly chosen positions to M walkers.
while stopping criterion not achieved
  for each walker
    Shift the walker to a new position.
    Calculate p.
    if p<1
      The new position is accepted with probability p.
    else
      The new position is accepted.
    end if
  end for
end while

```

Each walker is a coordinate vector R , for example $R = (r_1, \theta_1, r_2, \theta_2, \dots)$, where r_i and θ_i are the radial and angular coordinates of particle i . The variable p is equal to $|\Psi_\alpha(R')|^2/|\Psi_\alpha(R)|^2$, where R' is the new and R the old coordinate vector. To avoid the effect that possibly a walker can get stuck into a limited region, one normally uses more than one random walker. The use of several independent walkers also enables to do a rigorous error analysis.

The average of an observable A can be estimated as the mean of the estimates obtained by each of the N_W walkers, i.e.

$$\langle A \rangle = \sum_{i=1}^{N_W} \frac{\langle a \rangle_i}{N_W}, \quad (3.17)$$

where $\langle a \rangle_i$ is the mean of the observable A calculated over N time steps for walker i . The central limit theorem gives an error estimate of A

$$\epsilon = \frac{\sigma}{\sqrt{N_W}}, \quad (3.18)$$

where

$$\sigma = \sqrt{\sum_{i=1}^{N_W} \frac{(\langle a \rangle_i - \langle A \rangle)^2}{N_W}}. \quad (3.19)$$

If the calculations are done with only a single walker, the error can be estimated by data-blocking [50]. The data sequence is then divided into blocks of equal size larger than the correlation time, averages are calculated in each block, and the error is estimated as the standard deviation of the uncorrelated block averages.

3.2.5 Optimization of trial wave functions

In the third step of the variational method presented in Subsec. 3.2.1, the variational parameters of the trial wave function $\Psi_\alpha(R)$ are updated. In our calculations, we minimize the energy estimate $\langle E \rangle = E[\Psi_\alpha]$. Another possibility would have been to minimize the variance of the local energy. The variance minimization method has the advantage that it is numerically stable, and the minimum value is exactly known [53]. Its drawback is that a variance minimum point need not to correspond to the energy minimum. According to Siljamäki *et al.* [53], the stochastic gradient approximation (SGA) method [54] has overcome most of the numerical stability problems associated with energy minimization, and the energy minimization approach is therefore to prefer. Here we will concentrate on the energy minimization case, since we use that approach.

As shown by Lin *et al.* [55], the analytic first derivative of the energy E with respect to a variational parameter α_i can be calculated from the formula²

$$\frac{\partial E}{\partial \alpha_i} = 2\Re \left\{ \left\langle E_L \frac{\Psi'}{\Psi} \right\rangle - \langle E_L \rangle \left\langle \frac{\Psi'}{\Psi} \right\rangle \right\}, \quad (3.20)$$

²The formula here is generalized to the case when the wave function is complex, whereas Lin *et al.* presented a formula for the case when the wave function is real.

where $\Psi' = \partial\Psi/\partial\alpha_i$, $\Re\{\cdot\}$ denotes the real part and the angle brackets denote mean values calculated over a configuration set. In this work, the averages are calculated using Eq. (3.17).

We use the stochastic gradient approximation (SGA) method [54] to optimize the energy. The SGA approximation takes advantage of the stochastic noise inherent in the Metropolis method. In the specific case of optimization of the energy, the variables α are updated according to

$$\alpha_{i+1} = \alpha_i - \gamma_i \nabla_\alpha E, \quad (3.21)$$

where we calculate the components of $\nabla_\alpha E$ with the formula (3.20). The step length γ_i is dynamically changed and is determined by $\gamma_i = \gamma_0 i^{-k}$, where γ_0 and k are adjustable parameters. The parameter k has to satisfy the condition $\frac{1}{2} < k \leq 1$ [53, 54]. The condition is needed to ensure that the cumulative error of the noise in the approximative gradient dissipates and to ensure that the parameters α can reach infinitely far from their respective starting points.

3.2.6 Variational trial wave functions

In the VMC many-body calculations, we use variational wave functions of the Slater-Jastrow type

$$\Psi = D_\uparrow D_\downarrow \prod_{i < j}^N J(r_{ij}), \quad (3.22)$$

where D_\uparrow and D_\downarrow are Slater determinants of the single-electron states for the respective spin types, and J is a Jastrow two-body correlation factor [38]. In a two-dimensional system, the electrons have less degrees of freedom to avoid each other than in a higher-dimensional system. This enhances the inter-electron correlations. On the other hand, in a two-dimensional system it becomes more difficult for more than two electrons to get close to each other, and the relative importance of three-body and higher-order correlations become smaller than in a 3D system [23]. Therefore, in our calculations we have neglected other than two-body correlations. The used Jastrow factor was of the type

$$J(r_{ij}) = \exp \left[\frac{C r_{ij}}{\alpha_{ij}(1 + \beta_{ij} r_{ij})} \right], \quad (3.23)$$

where C is the Coulomb strength ($C = 1$ in effective atomic units) and β_{ij} is a variational parameter that is different for parallel and antiparallel

spin pairs, but due to symmetry the same for all pairs with the same spin polarization. These two β_{ij} parameters depend on the magnetic field B , and the wave function must therefore be optimized separately with respect to these parameters for each magnetic field value. The parameter α_{ij} is determined by the cusp condition, i.e. the condition necessary to ensure that the Hamiltonian equation has no singularities as the interparticle distance r_{ij} approaches zero. In a two-dimensional electron system the cusp condition can be shown to be [53]

$$\frac{\partial_r J}{J} = \frac{C}{2\delta_{\sigma_i, \sigma_j} + 1}, \quad (3.24)$$

where σ_i is the spin direction of particle i , $\delta_{\sigma_i, \sigma_j}$ is the Kronecker delta function, and $\partial_r = \partial/\partial r$. With the chosen Jastrow function, the left hand side of Eq. (3.24) becomes

$$\frac{\partial_r J}{J} = \frac{C}{\alpha_{ij}(1 + \beta_{ij}r)^2} \xrightarrow{r \rightarrow 0} \frac{C}{\alpha_{ij}}. \quad (3.25)$$

Substituting this expression into the cusp condition (3.24), we get $\alpha_{ij} = 2\delta_{\sigma_i, \sigma_j} + 1$.

For the Slater determinants, we use single-particle wave functions of the form (3.2), with the exponential factor $\exp(-r^2)$ replaced with the factor $\exp(-\gamma r^2)$, where γ is a variational parameter. All in all, the many-electron trial wave function (3.22) may be written

$$\Psi \equiv \Psi(\beta_{\uparrow\uparrow}, \beta_{\uparrow\downarrow}, \gamma), \quad (3.26)$$

where $\beta_{\uparrow\uparrow}$, $\beta_{\uparrow\downarrow}$ and γ are the variational parameters. The effect of the Jastrow factor is to include contributions from Landau levels higher than the lowest one. In studies by Harju *et al.* [56], the Jastrow function of Eq. (3.23) was able to capture up to 98 % of the Landau-level mixing in a three-electron quantum dot.

3.2.7 Multi-configuration states

Let us first consider a non-interacting many-particle system. Let

$$|m_i s_i n_i; N\rangle := |m_1 \cdots m_N s_1 \cdots s_N n'_1 \cdots n'_N\rangle \quad (3.27)$$

be a Slater determinant made up of single-particle eigenstates of the Hamiltonian

$$H_i = \frac{(-i\hbar\nabla_i + e\mathbf{A})^2}{2m^*} + V(r_i), \quad (3.28)$$

where each single-particle state has the angular momentum m_i , spin s_i and Landau level n'_i . The set of possible eigenfunctions (3.27) form a complete orthonormal basis in the Hilbert space defined by the Hamiltonian

$$H = \sum_i^N H_i. \quad (3.29)$$

Using Eq. (2.36) and the relation $L_z = \sum_{i=1}^N L_z^{(i)}$ for the total angular momentum operator, we get ($\hbar = 1$)

$$L_z |m_i s_i n'_i; N\rangle = \left(\sum_{i=1}^N m_i \right) |m_i s_i n'_i; N\rangle. \quad (3.30)$$

Thus, the total orbital angular momentum quantum number $m = \sum_{i=1}^N m_i$. Similarly, the total spin in the direction of the magnetic field $s = \sum_{i=1}^N s_i$, where s_i is the spin of particle i .

Let us denote the N -particle eigenstate of the Hamiltonian H with the quantum numbers m and s as $|ms\rangle$. Due to the completeness and orthonormality of the eigenfunctions (3.27), we may write $|ms\rangle$ as a linear combination

$$|ms\rangle = \sum_{m=\sum_i m_i} \sum_{s=\sum_i s_i} \sum_{n'_i} |m_i s_i n'_i; N\rangle \langle m_i s_i n'_i; N | ms\rangle, \quad (3.31)$$

where the summation is taken over all combinations with total angular momentum m , all combinations with total spin s and over all possible Landau levels $n'_i = \{0, 1, 2, \dots\}$, $i = \{1, 2, \dots, N\}$. The integrals

$$\langle m_1 \dots m_N s_1 \dots s_N n'_1 \dots n'_N | ms\rangle \quad (3.32)$$

are generalizations of the so-called *Clebsch-Gordan coefficients* [43]. These coefficients can in principle be obtained by using general properties of angular momentum operators and eigenstates [43, 57].

When introducing interactions, for example the pure Coulomb interaction, between the particles, the situation becomes considerably more complicated. As stated above, in our VMC-calculations we have approximated the interacting single-configuration N -particle state with the Slater-Jastrow function Ψ of Eq. (3.22). Let $\Psi_i = \mathfrak{D}^{(i)} \mathfrak{J}$ be a given configuration of the state Ψ , where $\mathfrak{D}^{(i)}$ is the Slater factor and \mathfrak{J} the Jastrow factor. Then, a linear combination of all possible configurations Ψ_i may be written

$$\sum_i \alpha_i \Psi_i = \left(\sum_i \alpha_i \mathfrak{D}^{(i)} \right) \mathfrak{J}, \quad (3.33)$$

where α_i are complex coefficients. By the completeness of the Slater-type configurations, we see that the basis $\{\Psi_i\}_i$ is also complete. Correspondingly, we may express an arbitrary interacting state $|ms\rangle$ as a linear combination of single-configuration states, but now the coefficients of Eq. (3.31) are determined also by the interaction effects in the system.

3.3 Exact diagonalization

The Hamiltonian of an N -electron system can usually be written in the form

$$\hat{H} = \hat{T} + \hat{U}, \quad (3.34)$$

where \hat{T} is the single-particle part and \hat{U} the two-particle part of the Hamiltonian. Let $\{|\phi_i\rangle\}_{i=1}^{N_B}$ be an arbitrary complete orthonormal basis of the given Hilbert space. Then, the eigenvalue equation of the Hamiltonian \hat{H} can be written in the matrix representation as

$$\mathbf{H}\mathbf{c} = E\mathbf{c}, \quad (3.35)$$

where \mathbf{H} is a matrix with the matrix elements $H_{nm} = \langle\phi_n|\hat{H}|\phi_m\rangle$, \mathbf{c} is a vector with elements $(c_n)_{n=1}^{N_B}$, and E is the energy of the system. By solving this matrix eigenvalue equation, the exact solution of the Hamiltonian equation can *ideally* be calculated and the eigenstate $|\psi\rangle$ is the linear combination of the basis states $|\phi_i\rangle$,

$$|\psi\rangle = \sum_{i=1}^{N_B} c_i |\phi_i\rangle. \quad (3.36)$$

In real computations, only a finite number of basis functions can be included. This is the most basic idea of the exact diagonalization (ED) method.

In the ED method, the basis states $|\phi_i\rangle$ are chosen to be N -electron eigenstates of the single-particle Hamiltonian \hat{T} . The basis states are Slater determinants

$$|\phi_i\rangle = \text{Slater}(\{|\varphi_j\rangle, j \in \mathcal{S}\}), \quad (3.37)$$

where the N different single-particle wave functions $|\varphi_j\rangle$ are eigenstates of \hat{T} , and \mathcal{S} is a set of N indices, as chosen among totally M possible states. The total number of basis states $|\phi_i\rangle$ is thus the number of possible combinations $N_B = \binom{M}{N}$. A basis function $|\phi_\alpha\rangle$ can be written in the occupation number representation as

$$|\Phi_\alpha\rangle = |n_{\alpha 1}, n_{\alpha 2}, \dots, n_{\alpha M}\rangle, \quad (3.38)$$

where $n_{\alpha j}$ is the number of particles in the state j . The Pauli exclusion principle sets the restriction $n_{\alpha j} \in \{0, 1\}$ for fermions. N states have to be occupied and the rest unoccupied.

To solve the eigenvalue equation (3.35), the matrix elements H_{nm} must be calculated first. In second quantization, the single-particle operator can be written [58]

$$\hat{T} = \sum_{i,j} t_{ij} c_i^\dagger c_j, \quad (3.39)$$

where

$$t_{ij} = \langle i | \hat{t} | j \rangle = \int d\mathbf{r} \varphi_i^*(\mathbf{r}) t(\mathbf{r}) \varphi_j(\mathbf{r}), \quad (3.40)$$

the states $|i\rangle \hat{=} \varphi_i(\mathbf{r})$ are single-particle basis functions and $\hat{t} \hat{=} t(\mathbf{r})$ is the single-particle operator. The creation operator c_i^\dagger increases the number of particles in state i by one and the annihilation operator decreases the same number by one. Similar to the one-particle part, the two-particle operator can be written

$$\hat{U} = \frac{1}{2} \sum_{i,j,k,l} \langle ij | \hat{v} | kl \rangle c_i^\dagger c_j^\dagger c_l c_k, \quad (3.41)$$

where

$$\begin{aligned} \langle ij | \hat{v} | kl \rangle &= v_{ijkl} \\ &= \delta_{\sigma_i, \sigma_k} \delta_{\sigma_j, \sigma_l} \int d\mathbf{r} \int d\mathbf{r}' \varphi_i^*(\mathbf{r}) \varphi_j^*(\mathbf{r}') v(\mathbf{r}, \mathbf{r}') \varphi_k(\mathbf{r}) \varphi_l(\mathbf{r}'), \end{aligned} \quad (3.42)$$

the states $|i\rangle$ are single-particle basis functions, and $v(\mathbf{r}, \mathbf{r}')$ is the two-particle operator in the coordinate representation.

As the single-particle basis functions $|i\rangle$ in this case are eigenstates of \hat{t} , the single-particle parts of the matrix elements are [59]

$$T_{\alpha\beta} = \langle \Phi_\alpha | \hat{T} | \Phi_\beta \rangle = \delta_{\alpha\beta} \sum_i n_{\alpha i} \varepsilon_i, \quad (3.43)$$

where ε_i are single-particle energy eigenvalues. The two-particle parts of the matrix elements

$$U_{\alpha\beta} = \langle \Phi_\alpha | \hat{U} | \Phi_\beta \rangle \quad (3.44)$$

are derived in detail in Ref. [59] using the properties of creation and annihilation operators. These elements are different sums of v_{ijkl} terms, as defined in Eq. (3.42), multiplied by $n_{\alpha i}$ terms. The reader may consult Appendix A for details on how the interaction matrix elements v_{ijkl} are evaluated in our simulations.

The total number of basis functions N_B can be reduced by fixing, for example, the z -component of the total spin and/or angular momentum. The Hamiltonian matrix is finally diagonalized. In our calculations, we use the Lanczos diagonalization procedure [60]. This is a very efficient method when the matrix is sparse and we are interested in only the smallest eigenvalue, i.e. the energy ground state. The most serious restriction of the ED method is that, due to exponential growth of the basis size as a function of the number of electrons N , the computational cost scales exponentially as a function of the electron number. In practice the bad scaling can be seen by that whence a four-electron calculation needed a few minutes of CPU time, a six-electron calculation lasted several hours. As will be seen in Sec. 4.3, the convergence as a function of the number of single-electron states M may also be slow. Depending on the basis size needed in the calculations, the ED method is therefore normally used only for systems with up to 6-10 electrons [59].

Chapter 4

Computational results

In this chapter, we present the numerical results of this Thesis. First, in Sec. 4.2, we present the single-electron energy spectra of three different test case quantum dots. In Subsec. 4.3.2 we compare the energy ground states of four different systems calculated with the VMC and ED methods, respectively. Later, in Subsecs. 4.3.3, 4.3.4 and 4.3.5, we compare the spin structure of different four- and six-electron systems, as obtained with the ED method. We also study the vortex structure of the quantum dots using conditional wave functions, which depict the structure of the $2N$ -dimensional wave function in a 2-dimensional subspace.

4.1 Confinement potentials

In this Master's Thesis, we studied few-electron quantum dots with a few different circular confinement potentials. The test cases are presented in Tab. 4.1 and plotted in Fig. 4.1. The r^8 potential is interesting as an intermediate case between a circular hard-wall and a parabolic potential. Few-electron quantum dot systems with the latter two potentials are quite well known, and for example the spin as a function of the magnetic field has been calculated previously for those cases [17, 61, 62]. Parabolic ring potentials of the type 2 given in Tab. 4.1 have commonly been used to model quantum rings [10, 63, 64]. There is no profound reason behind the exact shape of the chosen r^6 +Gaussian confinement potential, but the very strong Gaussian perturbation around the origin combined with the steep r^6 part makes the ring very narrow, considerably narrower than the rather wide parabolic ring also used here (see Fig. 4.1). The r^2 +Gaussian potential was used with different perturbation strengths V_0 . These potentials were used to model an electrostatically induced continuous transition from a pure parabolic

Table 4.1: Our test cases of non-parabolic confinement potentials, given in effective atomic units. m^* is the effective mass and \hbar is Planck's constant. Where no units are given, it means the effective atomic units.

	Case	Potential	Parameters
1	r^8	$V(r) = \alpha r^8$	$\alpha = 0.27^8$
2	Parabolic ring	$V(r) = \frac{1}{2}m^*\omega_0(r - r_0)^2$	$\hbar\omega_0 = 3.5$ meV, $r_0 = 8/\pi$
3	r^6 +Gaussian	$V(r) = \alpha r^6$ $+V_0 \exp(-r^2/\sigma^2)$	$\alpha = 0.27^6$, $V_0 = 4$, $\sigma = 2$
4	r^2 +Gaussian	$V(r) = \frac{1}{2}m^*\omega_0 r^2$ $+V_0 \exp(-r^2/\sigma^2)$	$\hbar\omega_0 = 5$ meV, $\sigma = 2$
5	r^2 +shifted Gaussian	$V(r) = \frac{1}{2}m^*\omega_0 r^2$ $+V_0 \exp(-(r - r_0)^2/\sigma^2)$	$\hbar\omega_0 = 5$ meV, $\sigma = 0.25$, $r_0 = 2$

dot to a ringlike system. Similarly, the r^2 +shifted Gaussian potential of Tab. 4.1 was used to model a transition from a parabolic dot to a coupled dot–ring system (see Fig.4.1). For comparison, we have also studied the well-known parabolic quantum dot with 5 meV confinement strength.

4.2 Single-electron systems

The single-electron states of the systems with non-parabolic confinement potentials were calculated as explained in Sec. 3.1. The potential-difference integrals of Eq. (3.5) were solved numerically using a standard MATLAB routine. In all the considered cases, both the single-particle wave functions $\phi_{n'}^l$ and the corresponding energies were found to converge well with 15 basis functions. We therefore used 15 basis functions in all our calculations when solving the single-electron coefficients of Eq. (3.3).

In Figs. 4.1 (b) and 4.2, single-electron energy spectra as functions of the magnetic field for the confinement potential cases 1, 2 and 3 of Tab. 4.1 are presented. The single-electron energy spectrum of the r^8 case reminds strongly of the hard-wall potential case, as given in Ref. [23]. Both in the hard-wall and the r^8 system the degeneracy at zero magnetic field is broken, when compared to the parabolic case. The same kind of broken degeneracy at zero magnetic field is also present in the parabolic ring case (Fig. 4.2 (a)). As opposed to the r^8 dot, in the parabolic quantum ring the $l = 0$ total angular momentum state (the lowest energy band at $B = 0$) is not the ground

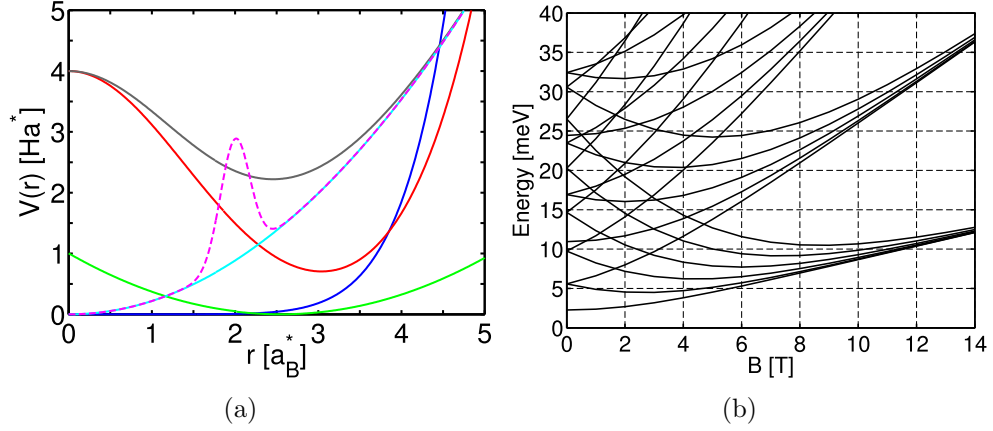


Figure 4.1: (a) The different confinement potentials of Tab. 4.1. The potentials are r^8 (blue), parabolic ring (green), $r^6 + \text{Gaussian}$ (red), $r^2 + \text{Gaussian}$ (grey), $r^2 + \text{shifted Gaussian}$ (magenta) and 5 meV parabolic (cyan). (b) Single-electron energy spectrum as a function of the magnetic field for the r^8 confinement potential of Tab. 4.1.

state at high magnetic fields. In the $r^6 + \text{Gaussian}$ confinement potential case, band crossings in the ground state is more pronounced. The single-electron spectrum of the $r^6 + \text{Gaussian}$ system is similar to that obtained with narrow parabolic ring confinement models in Ref. [64]. The energy spectrum approaches the periodic structure present in a strictly one-dimensional quantum ring [64],

$$E_n(B) = \frac{\hbar^2}{2m^*r_0^2} \left(n + \frac{\Phi}{\Phi_0} \right)^2, \quad (4.1)$$

where r_0 is the radius of the ring, $\Phi = \pi r_0^2 B$ is the magnetic flux through the ring, Φ_0 is the Dirac flux quantum and n is an integer. The periodicity of the energy as a function of the magnetic field is a manifestation of the Aharonov–Bohm effect [14, 59].

4.3 Few-electron droplets

4.3.1 Technical details of the calculations

For all the potentials used, the two- and four-electron ED calculations were found to converge reasonably well at all considered magnetic field values when using 25 single-electron states (the variable M in Sec. 3.3). We therefore

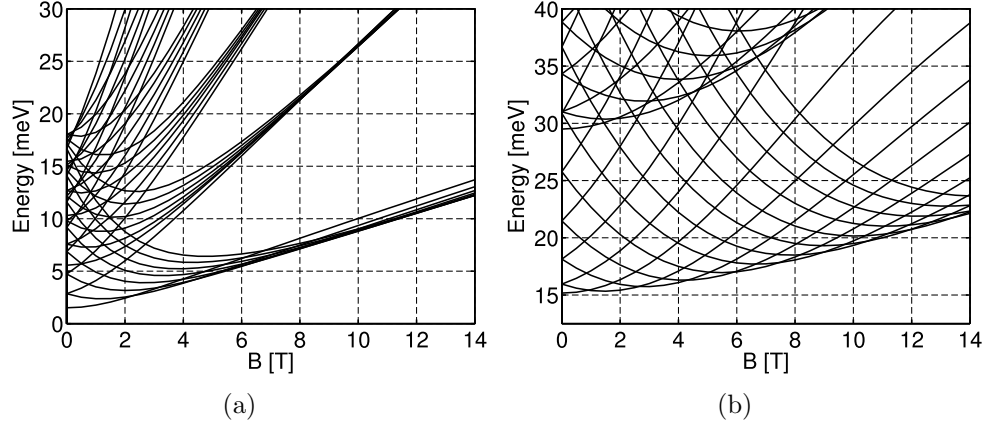


Figure 4.2: Single-electron energy spectrum as a function of the magnetic field for (a) the parabolic ring and (b) the r^6 +Gaussian confinement potentials of Tab. 4.1. The parabolic ring is wider than the r^6 +Gaussian system.

included the 25 lowest-lying single-electron states in all our calculations. As will be seen later, 25 single-electron states was not always sufficient in the six-electron calculations. For four-electron systems, the difference in energy between a calculation with 25 and 28 single-electron states was always found to be less than 0.12 meV, or approximately 1 per thousand of the total energy value.

The number of random walkers in the VMC calculations was fixed to 5, based on our convergence tests. In Ref. [54] they also found that the stochastic gradient approximation optimization converges most efficiently with the order of one random walker configurations, since then the method can take best advantage of the stochastic noise inherent in the calculations. In the VMC calculations, the error was estimated according to Eq. (3.18). When calculating the ground state energy of a 5 meV 4 electrons parabolic dot, the error bars of the VMC calculations were less than 0.05 meV, or less than approximately 1 per thousand of the total energy. The same relative accuracy was found for example with the r^6 +Gaussian confinement of Tab. 4.1. On the other hand, the standard deviation in the parabolic dot case was less than about 1/40 of the total energy, whereas it for the r^6 +Gaussian case was as large as 1/20 of the total energy.

In all our calculations, the Zeeman term was left out in order to enhance the spin effects. This can be justified physically since, as stated in Subsec. 2.5.4, the Zeeman term can be made vanishingly small in experiments.

As shown in Subsec. 2.3.2, in the high magnetic field limit the Landau inter-level separation increases directly proportionally to B . Therefore, the

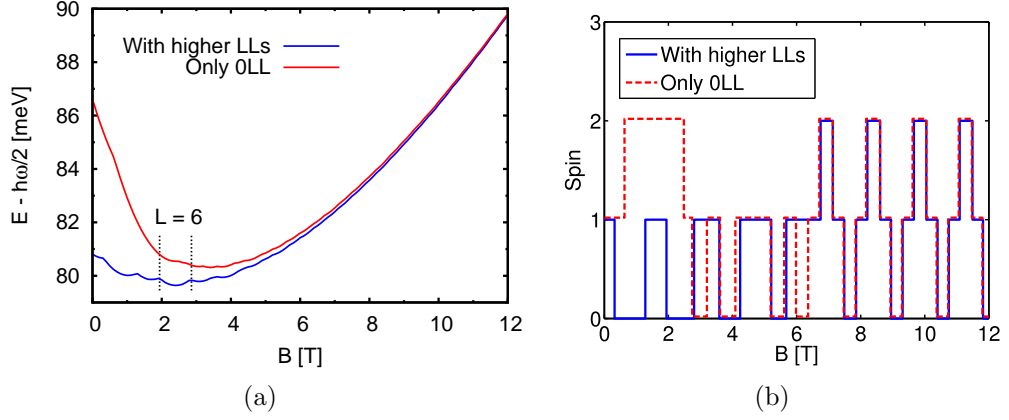


Figure 4.3: Comparison between the LLL approximation and a calculation with Landau level mixing included. Left: Ground state energy of a quantum dot with the r^6 +Gaussian electrostatic potential of Tab. 4.1. Right: Spin as a function of the magnetic field.

difference in energy between subsequent Landau levels becomes infinitely large when the magnetic field goes towards infinity. This makes only the lowest Landau level (LLL) important. It is a common approximation to include only the LLL single-particle states in calculations of parabolic dots at magnetic fields above the MDD region [10, 62]. Because of the proportionality to B of the inter-level separation, the approximation is found to improve for increasing magnetic fields.

In the calculations of this Thesis, we have investigated systems in the magnetic field range from zero Tesla up to values where the $\nu = 1/3$ filling fraction is found. In Figs. 4.3 and 4.4, we have compared the ground state energy and spin as functions of the magnetic field between the LLL approximation and a calculation done with Landau-level mixing (LLM). These results show the same trend as obtained by Siljamäki *et al.* [62] in VMC calculations of a parabolic QD: The LLL approximation fails at magnetic fields close to the MDD state (marked by $L = 6$ in the figures), and the spin states of the LLL calculation are shifted towards lower magnetic field values with respect to the LLM results. It is, however, surprising to see that the LLL approximation is quite exact for high magnetic fields in the r^6 +Gaussian system. This is untrivial, since the Fock-Darwin states are not eigenstates of the single-particle system. Because of the failure of the LLL approximation, in particular at low magnetic fields, we have done all the following calculations using full Landau-level mixing.

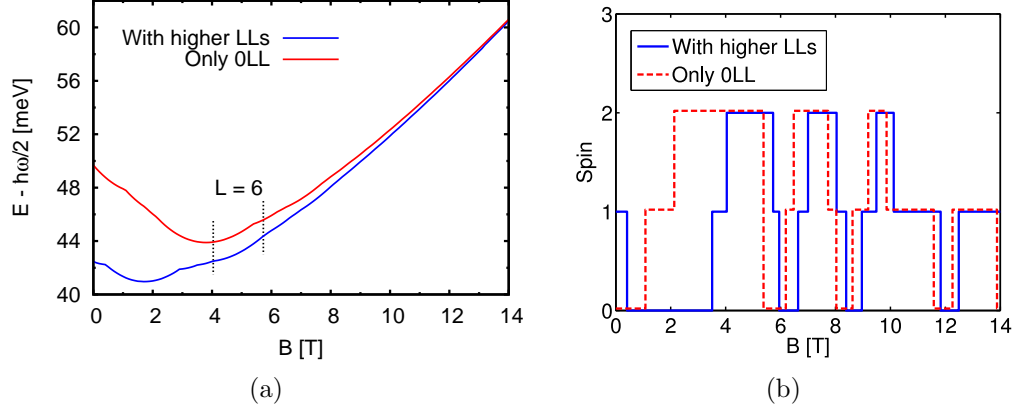


Figure 4.4: The same as Fig. 4.3, but for the r^8 potential of Tab. 4.1.

4.3.2 VMC ground states

As noted in Sec. 3.3, the computational cost of the ED method as a function of the number of electrons scales very badly. Therefore, it would be desirable to find another computational method to solve systems with general confinement potentials, circular symmetry and more than 6–8 electrons. Two methods that have been successfully implemented on quantum dot systems are density-functional theory (DFT) based methods [10, 65] and the VMC method (see Sec. 3.2). The DFT methods are powerful to study large systems, but a major drawback is that they are sometimes not able to calculate correlation effects very exactly. Symmetry considerations may also be highly nontrivial in these methods [66]. In DFT calculations, for example, different angular momentum eigenstates may be mixed in an unphysical way, because of limitations of the method [66]. The VMC method is in principle exact, if the trial wave function has the proper form. However, in many cases it is not obvious what is a good trial wave function for a given system. In the following, we are going to investigate how well single-configuration states of the form of Eq. (3.22) are able to capture the physics of different circular quantum dots.

We calculated ground state energies of a few systems using trial wave functions of the form of Eq. (3.22). Such a wave function corresponds to a fixed configuration of single-electron orbital angular momenta and spins. For each total angular momentum and spin, we have chosen the single configuration with lowest energy as the ground state candidate. In Figs. 4.5–4.8, the ground state energy is given as a function of the magnetic field for a four-electron 5 meV parabolic dot and for four-electron systems of the cases

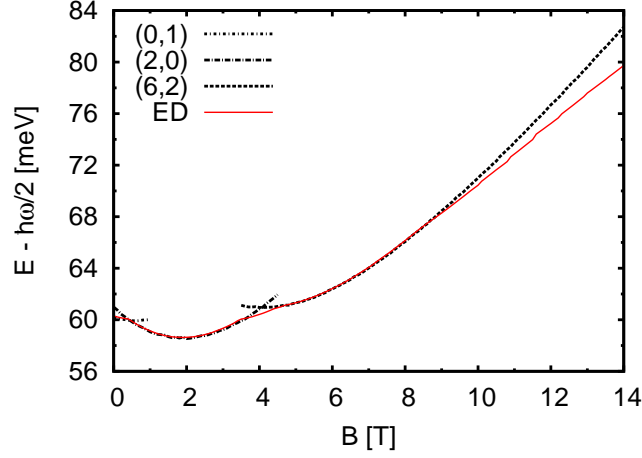


Figure 4.5: Ground state energy as a function of the magnetic field for a four-electron dot with a 5 meV parabolic confinement potential. The VMC ground states (black/dashed) are compared with the ED ground states (red/continuous line).

1–3 of Tab. 4.1. The VMC results are compared with the more accurate ED results. For the r^8 and r^6 +Gaussian systems, we have also included a DFT prediction of the energy value at zero magnetic field (see Figs. 4.6 and 4.8). Both the ED and the single-configuration VMC methods are more accurate than the used DFT method at 0 Tesla. For the parabolic, the r^8 , and the parabolic ring cases, the agreement between the ED and VMC methods was very good at magnetic field values up to the MDD region. However, the states $(L, S) = (4, 0)$ and $(5, 1)$ were ground states in the ED calculations, but not in the VMC calculations.

In the FQHE regime above the MDD region, the single-configuration VMC method clearly failed. This is in agreement with the spin polarized parabolic dot studies presented in Ref. [67]. The authors used the same kind of single-configuration wave functions as we have used, and conclude that the function becomes less accurate for larger angular momentum values, since the difference in energy between the different configurations then decreases. As seen from our results, the spin-unpolarized states behave considerably worse than the spin-polarized states.

The VMC ground state energy of the narrow, ring-shaped r^6 +Gaussian potential was not very accurate at any magnetic fields (see Fig. 4.8). At magnetic fields less than 7 T, the ground state energies of the VMC calculations were shifted from about 0.3 meV up to at most about 1 meV with

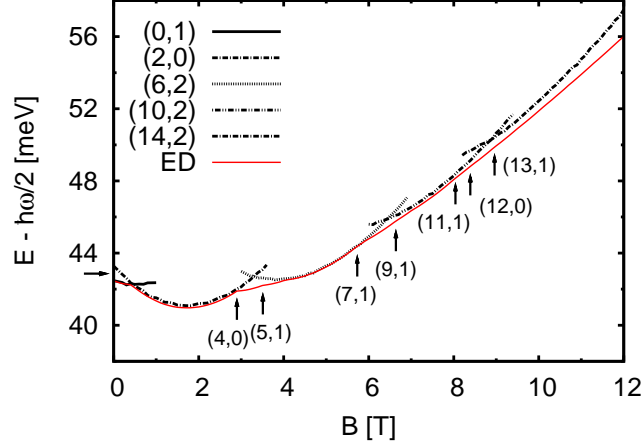
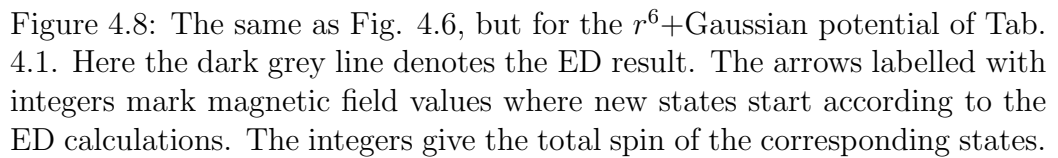
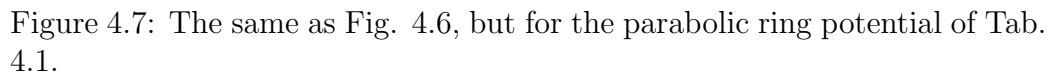


Figure 4.6: Ground state energy as a function of the magnetic field for a four-electron dot with the r^8 confinement potential of Tab. 4.1. The VMC results are denoted by (L, S) , where L is the total angular momentum and S the total spin, both in the direction of the external magnetic field. The exact diagonalization result is denoted by ED. The arrow pointing at the vertical axis shows the ground state energy at zero magnetic field, as obtained in a density functional theory (DFT) based calculation. The other arrows mark the lowest magnetic field values of those states obtained only with the ED method.

respect to the ED ground state energy.

In Figs. 4.6 and 4.7, we have marked with arrows those states that failed to become ground states in the VMC calculations. In Fig. 4.8, all ground states of the ED calculation are marked with an arrow. As one can see, even if the ground state energy is reasonable in all the different systems, the spin structure was almost completely lost in the VMC calculations. In Fig. 4.9, the relative weight of the most important configuration of the ED calculations is plotted as a function of the magnetic field. The spin values of the corresponding ground states are also given in the figures. By comparing the relative weights of the most important configuration with the obtained VMC ground states, one finds that the VMC method works well only when the relative weight of the most important configuration is larger than about 0.5. In opposite cases, the many-particle states can not be described well by a single-configuration trial wave function. The many-body states are found to be closest to single-configuration states, or, the single-configuration VMC calculations work best, when the system is spin polarized (Fig. 4.9).



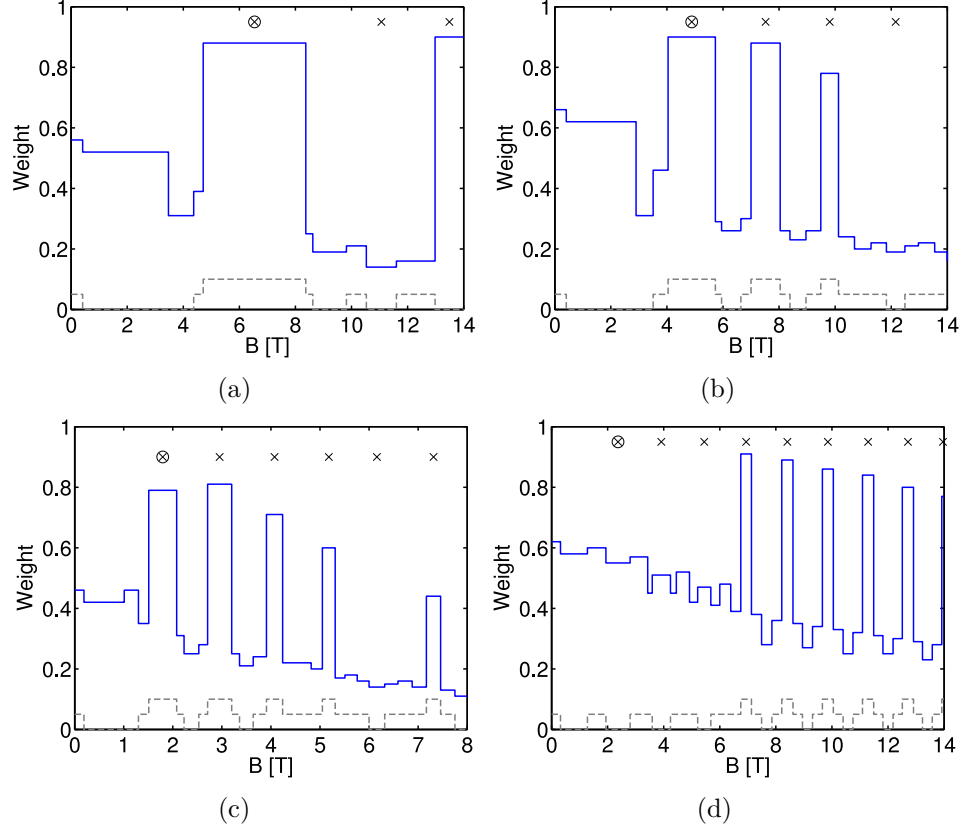


Figure 4.9: Relative weight of the most important configuration as a function of the magnetic field. The values are only approximate, as the value of the weights within a fixed (L, S) state change continuously as a function of the magnetic field B . The dashed grey line gives the spin values 0, 1 or 2 as a function of the magnetic field. The number of electrons is four and the confinement is (a) the 5meV parabolic, (b) the r^8 , (c) the parabolic ring, and (d) the r^6 +Gaussian potentials of Tab. 4.1. The crosses at certain magnetic field values denote the states for which $L = L_k \equiv L_{MDD} + kN$, where $L_{MDD} = N(N - 1)/2$ is the maximum-density droplet angular momentum, N is the number of electrons and $k \in \{0, 1, 2, \dots\}$. The MDD states are marked with a cross surrounded by a circle.

We conclude that even if single-configuration VMC calculations may work reasonably well for spin-polarized systems, that is not the case for a non-parabolic system with spin degree of freedom.

4.3.3 Spin structure

As stated in the previous subsection, the single-configuration VMC method was not able to give the right spin structure of a quantum dot with a general, non-parabolic potential. Therefore, in the following studies we have used only the ED method.

In Figs. 4.10 and 4.11, we have plotted the ground state spin and total angular momentum as functions of the magnetic field for different four-electron quantum dots. The considered systems are the 5 meV parabolic dot and the cases 1–3 of Tab. 4.1. The magnetization $M = -\partial E_{tot}/\partial B$, where E_{tot} is the ground state energy and B is the magnetic field, is also given as a function of the magnetic field. The crosses at certain magnetic field values in the spin plots denote the states for which $L = L_k \equiv L_{MDD} + kN$, where $L_{MDD} = N(N-1)/2$ is the maximum-density droplet angular momentum, N is the number of electrons and $k \in \{0, 1, 2, \dots\}$. The MDD states are marked with a cross surrounded by a circle. As seen from the figures, if the many-particle system is spin polarized, it happens always at some of the magic angular momenta L_k .

In the magnetic field range of Fig. 4.10 (a), the parabolic QD is spin polarized only in the $L = 6$ state, corresponding to the MDD state in the thermodynamic limit. The states with angular momenta $L = L_1$ and $L = L_2$ have zero spin. In the r^8 potential case of Fig. 4.10 (c), the states L_0 , L_1 and L_2 have spin 2, while the state L_3 is unpolarized. The spin structure of the r^8 system agrees mostly well with the circularly symmetric hard-wall case of Ref. [17], but the L_3 state is polarized in the hard-wall system, whereas in the r^8 dot it is unpolarized. It seems like higher and higher L_k states become spin polarized, as the potential changes continuously from parabolic to hard-wall. The same trend is seen for the parabolic ring case of Fig. 4.10 (e) and the r^6 +Gaussian case of Fig. 4.11 (a), where the potential becomes more ringlike. However, when the electrostatic confinement becomes sufficiently narrowly ring-shaped, low L_k states start to depolarize (see Fig. 4.11).

At low magnetic fields, the magic angular momentum states L_k can be seen in the magnetization plots as relatively large regions where the magnetization curve is smooth. However, there can be seen no obvious difference between spin polarized and unpolarized states. The narrower the quantum ring is, the more rapid are the oscillations in the magnetization as a function of the magnetic field. In the four-electron parabolic and r^8 cases, the non-

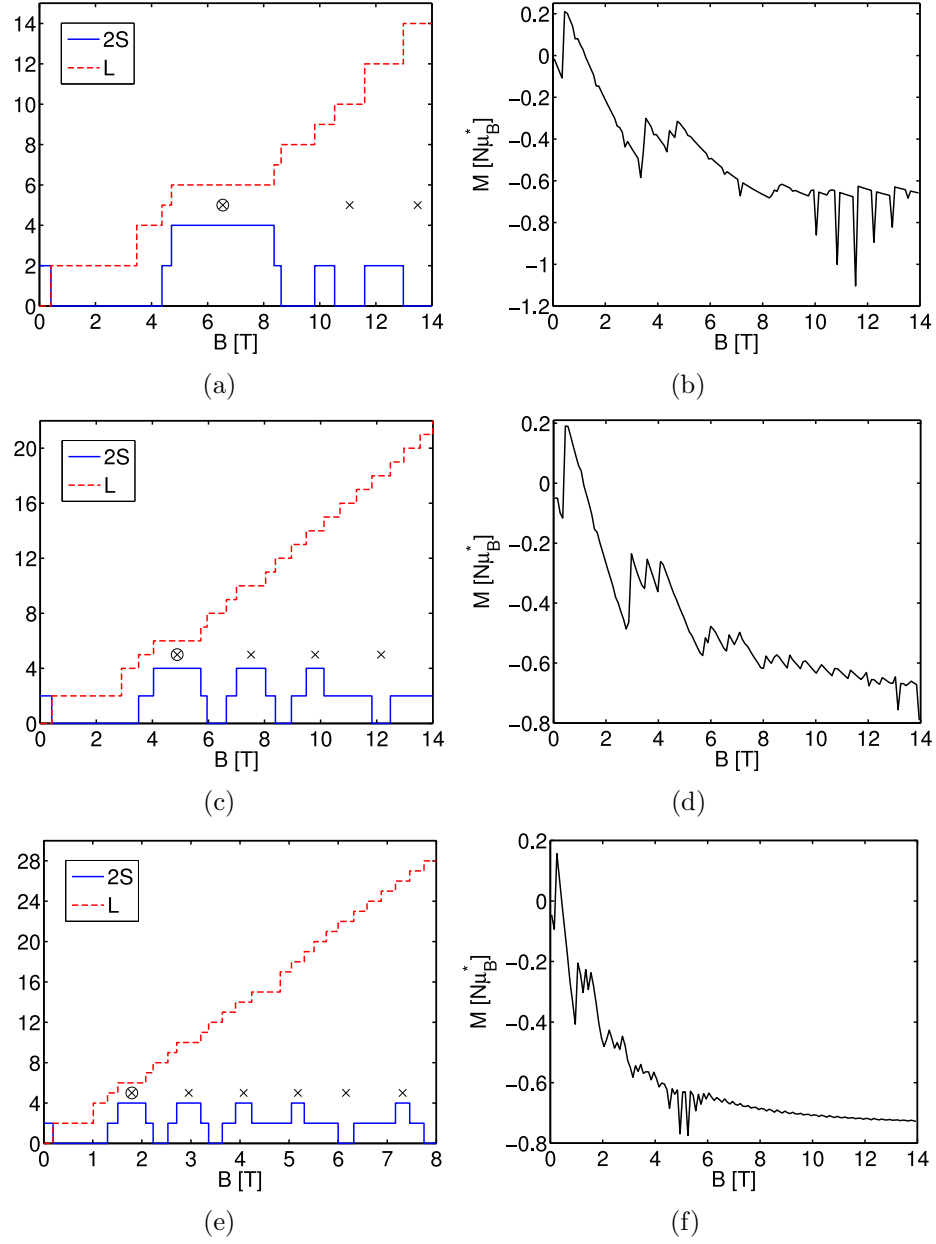


Figure 4.10: Left: Total angular momentum L and spin S as functions of the magnetic field for a four-electron quantum dot. Right: Magnetization M of the same dot, plotted as a function of the magnetic field. The magnetization is given in units of N times the Bohr magneton. The systems are (a)–(b) the 5 meV parabolic dot, (c)–(d) the r^8 , and (e)–(f) the parabolic ring dots of Tab. 4.1.

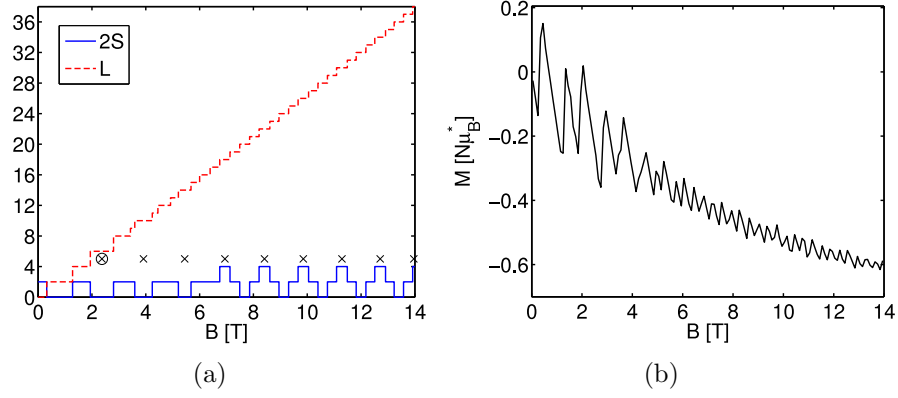


Figure 4.11: The same as Fig. 4.10, but for the r^6 +Gaussian potential of Tab. 4.1.

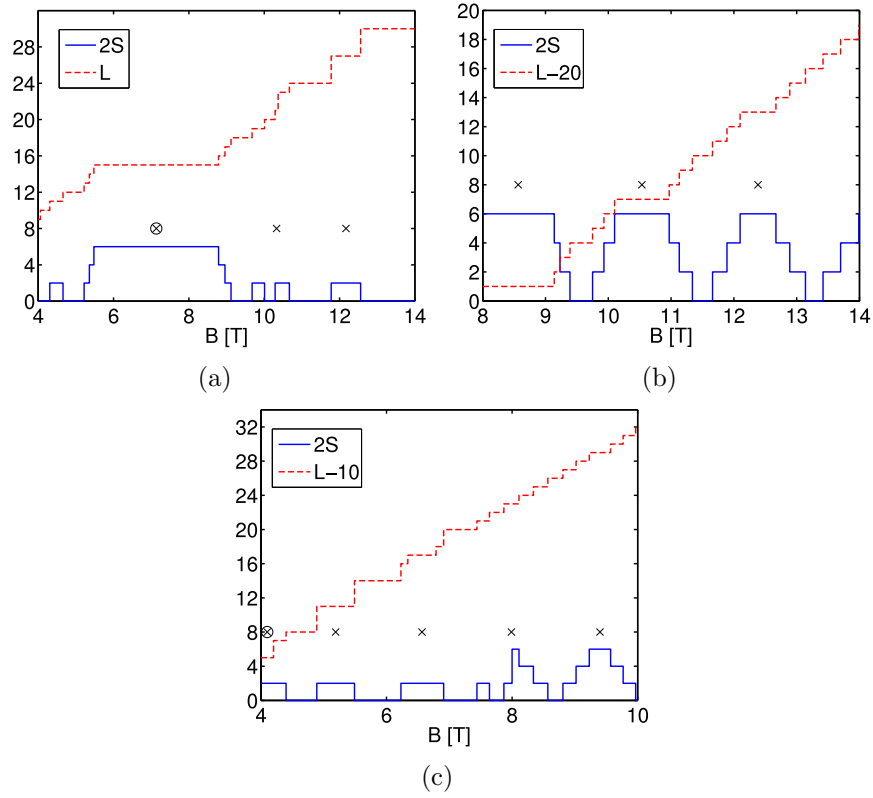


Figure 4.12: Ground state total angular momentum L and spin S , plotted as functions of the magnetic field for a six-electron quantum dot with (a) the 5 meV parabolic potential, (b) the r^8 , and (c) the r^6 +Gaussian potentials of Tab. 4.1.

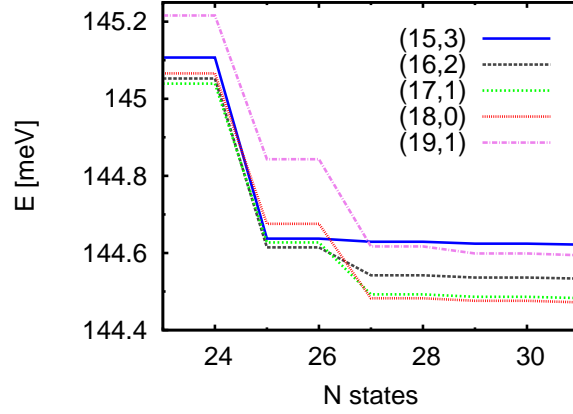


Figure 4.13: Energy of a six-electron 5 meV parabolic QD given as a function of the number of single-electron states used in the ED calculation. All the (L, S) states were calculated at the magnetic field 8.9 T.

interacting energy is a smooth function of the magnetic field (Figs. 2.4 and 4.1 (b)), and the oscillations seen in the magnetization is therefore a pure consequence of the Coulomb interaction [68, 69]. On the other hand, in the parabolic ring and r^6 +Gaussian cases, the non-interacting energy is no longer a smooth function of the magnetic field (Fig. 4.2), and the oscillations seen in the magnetization is not necessarily a pure Coulomb interaction effect.

In Fig. 4.12, the total spin and angular momentum are given as functions of the magnetic field for six-electron systems with the parabolic, r^8 and r^6 +Gaussian confinements. The calculations were done with 25 single-electron states. The most stable states were found to converge well with 25 single-electron states, but, as seen from Fig. 4.13, some of the less stable states have clearly not converged with 25 single-electron states. The six-electron calculations were really time-consuming; it took about one month to calculate the ground states of one system through the entire magnetic field range. Because of the computational cost, we were not able to study the systems at all magnetic field values with more single-electron states. The presented six-electron results must therefore be considered with caution.

Siljamäki *et al.* [62] studied the same parabolic six-electron system as we studied, with the only difference that the dielectric constant ϵ was 12.4, whereas we used the value 12.7. Siljamäki *et al.* did VMC calculations with only a LLL trial wave function, and they did also calculations where the LLL wave function was multiplied with a Jastrow factor to include effects of Landau-level mixing. In the VMC calculations with the LLL approxima-

tion, they reported (L, S) ground states $(15,3)$, $(16,2)$, $(17,1)$, and $(18,0)$ at zero Zeeman coupling. When LLM was included, the intermediate partially spin polarized states $(16,2)$ and $(17,1)$ were found to vanish. As seen from Fig. 4.12 (a), in our ED calculations with 25 single-electron states, the states $(16,2)$ and $(17,1)$ were included. However, when the number of single-electron states was increased to at least 27, these two partially spin polarized states were found to vanish (see Fig. 4.13). Thus, both in the VMC calculations of Ref. [62] and in our ED calculations the states $(16,2)$ and $(17,1)$ seem to have been only an artefact of numerical approximation. Koskinen *et al.* [28] studied the spin structure of a six-electron parabolic dot by using the LLL approximation of the ED method. They have not presented the results explicitly as a function of magnetic fields, but instead given the spin of different angular momentum states. The LLL spin states of Ref. [28] agree exactly with our results for angular momenta $11 \leq L \leq 29$, when we included LLM and used 25 single-electron states. However, we got the total spin value 0 at the angular momentum $L = 10$, whereas Koskinen *et al.* got spin 2. This difference may be a consequence of that the LLL approximation is not very good at low angular momenta (see Sec. 4.3.1).

Note that the difference in energy between some of the states in the six-electron case was very small: For example, the difference between the states $(17,1)$ and $(18,0)$ at 8.9 T was only 0.01 meV, when calculated with 31 single-electron states. That is less than 1 per ten thousand of the total energy value. At zero temperature the lowest-lying state is indeed the ground state, but in a real experimental situation at finite temperature the real state will be a superposition of several fixed angular momentum states close in energy.

To our knowledge, there exist no studies of four- or six-electron systems with the r^8 and r^6 +Gaussian potentials. Despite the above mentioned convergency problems, the results presented in Figs. 4.12 probably give the right overall picture. In all the different six-electron cases, roughly the same structure is seen as in the corresponding four-electron cases. In the parabolic case, L_k states above the MDD are unpolarized, whereas in the r^8 case they are polarized. In the r^8 system, in comparison to the 4-electron case higher L_k states are polarized in the six-electron case. One should notice that, since the same potentials were used in both cases, the particle density is higher in the six-electron system. This may partly explain why high L_k states in the six-electron case behave more like lower L_k states in the four-electron case, because inter-electron correlations increase with magnetic field and decrease with charge density. In the system with a r^6 +Gaussian confinement potential, the three lowest L_k states are unpolarized, like in the four-electron case. In the six-electron system, there is seen a mixed state; Part of the L_3 state is unpolarized and part of it is polarized. Similar to the r^8 system,

some high L_k states in the six-electron case behave like lower L_k states in the four-electron case.

4.3.4 Spin oscillations

In the previous subsection, we found that the spin states seem to change in a more or less systematic way as the system changes from a parabolic dot to a narrow ringlike system. To study systematically the transition from a pure parabolic quantum dot to a ringlike system, we used the r^2 +Gaussian confinement potential of Tab. 4.1. We investigated a four-electron system using the perturbation strengths $V_0 = 0, 1, 2, 3$ and 4. The obtained phase diagram of the spin states as a function of magnetic field and perturbation is given in Fig. 4.14. For a fixed perturbation strength, spin periodicity of the type 0-1-2-1 is seen in the magnetic field regions where the system becomes spin polarized. This is the four-particle spin sequence of the ferromagnetic Heisenberg model, as given in Tab. 2.1. Similarly, for perturbation strengths $V_0 \geq 1$, the spin periodicity 1-1-0-1 is seen at high magnetic fields. This spin sequence is that of the antiferromagnetic Heisenberg model for a four-particle system, as given in Tab. 2.1. Thus, for perturbation strengths $V_0 \geq 1$, we see phase borders between distinct regions with behaviour similar to the ferromagnetic or antiferromagnetic Heisenberg models. In agreement with the results of the potential cases 1–3 of Tab. 4.1, as presented in the previous subsection, one can observe that higher magic angular momentum states $L_k = L_{MDD} + kN$, $k \in \{0, 1, 2, \dots\}$, become spin polarized when the perturbation strength V_0 is increased. Similarly, the lowest L_k states become unpolarized when the potential becomes more ringlike. Because this spin effect is similar in these two different sets of systems, it seems like the phenomenon is only weakly dependent on details of the confinement potentials. The perhaps most important parameter is the width of the (quasi)ring. Interestingly, all high L_k states are not unpolarized. Consequently, oscillations between spin polarized and unpolarized states is seen for fixed angular momenta. For example, the angular momentum state $L = 18$ had spin 2 when the perturbation strength V_0 was 0, spin 0 when V_0 was 1, and spin 2 again when V_0 was 2. These spin oscillations at constant angular momenta can be interpreted as quantum phase transitions between regions with spin structure similar to the ferromagnetic and antiferromagnetic Heisenberg models, respectively. We observe that there are not only one ferromagnetic and one antiferromagnetic region, but instead there seem to be periodically occurring bands of ferromagnetic and antiferromagnetic regions. In Subsec. 4.3.3, we found that the r^6 +Gaussian narrow ring had the antiferromagnetic Heisenberg model spin periodicity 1-1-0-1 at magnetic fields below 6 T. We assume

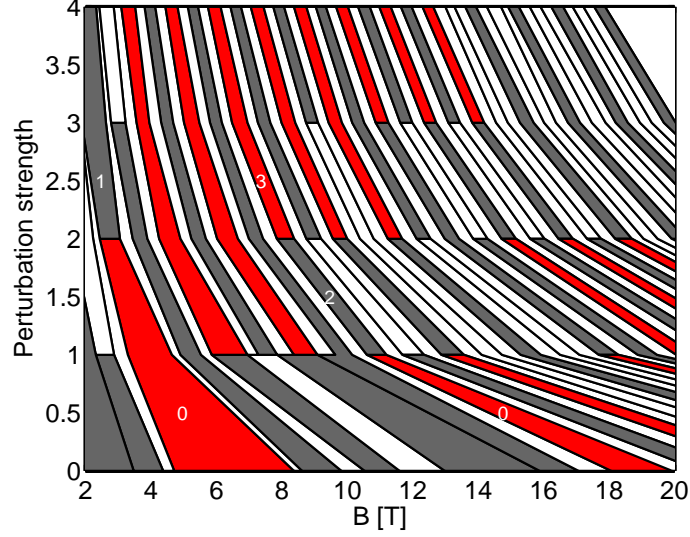


Figure 4.14: Phase diagram of the ground-state spin polarization as a function of the perturbation strength V_0 and magnetic field B . The four-electron quantum dot was restricted electrostatically by the r^2 +Gaussian potential of Tab. 4.1. The spin states are 0 (gray), 1 (white) and 2 (red). The more or less vertical bands seen in the diagram are different total angular momentum states. Observe the 2-0-2 spin oscillations obtained as a function of the perturbation strength V_0 for fixed total angular momenta. The numbers in the phase diagram denote the number of off-particle vortices created at the center of the dot. The broad region on the left-hand side with $S = 2$ is the MDD state with $L = 6$. The next spin polarized state at $V_0 = 0$ is the state $L = 18$.

that such an antiferromagnetic region at low magnetic fields is present also in the r^2 +Gaussian system for sufficiently large perturbation strengths.

To analyse the nodal structure of different systems, we calculated conditional wave functions. The conditional wave function of an N -particle system is defined as [66]

$$\psi_c(\mathbf{r}) = \frac{\Psi(\mathbf{r}, \mathbf{r}_2^*, \dots, \mathbf{r}_N^*)}{\Psi(\mathbf{r}_1^*, \mathbf{r}_2^*, \dots, \mathbf{r}_N^*)}, \quad (4.2)$$

where \mathbf{r} is the position of particle 1, and \mathbf{r}_i^* is the most probable position of particle i , as given by the total electron density $|\Psi|^2$. The phase θ is obtained from the relation $\psi_c(\mathbf{r}) = |\psi_c(\mathbf{r})| \exp(i\theta(\mathbf{r}))$ and the conditional electron density is defined as $|\psi_c(\mathbf{r})|^2$.

In Figs. 4.15 and 4.16, we have presented conditional wave functions of

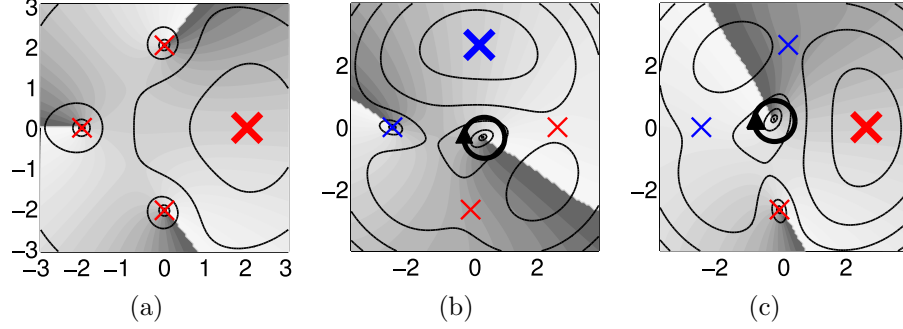


Figure 4.15: Conditional wave function consisting of the charge density, plotted with contour lines (logarithmic scale), and the phase of the wave function, illustrated by the gray-scale shading. The crosses mark the most probable electron positions and the circles with an arrow mark nodes. The probe electron is marked with a larger cross, and red and blue crosses denote the two spin directions, respectively. The angular momentum state $L = 6$ of the r^2 +Gaussian system of Tab. 4.1 is given for two different perturbation strengths V_0 : (a) $V_0 = 0$, $B = 6$ T, and $S = 2$. This state is the microscopic counterpart of the $\nu = 1$ QH state occurring in the thermodynamical limit. (b)–(c) $V_0 = 2$, $B = 3$ T, and $S = 0$. The state can be interpreted as a microscopic counterpart of the integer QH state $\nu = 2$ with one vortex added at the center of mass.

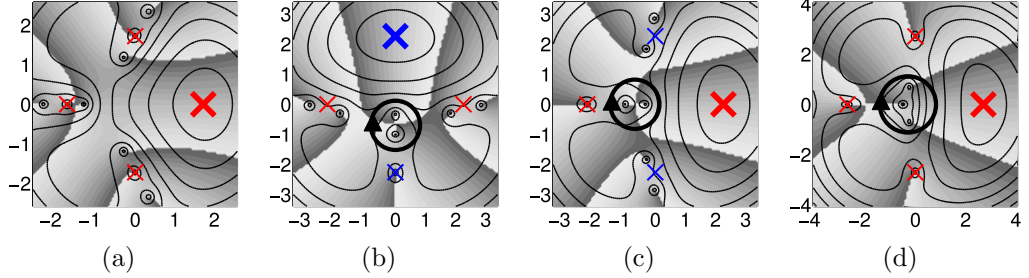


Figure 4.16: Conditional wave function, consisting of charge density and phase, as in Fig. 4.15, for the angular momentum state $L = 18$ of the r^2 +Gaussian system of Tab. 4.1. The system is plotted for three different perturbation strengths V_0 : (a) $V_0 = 0$, $B = 19$ T, and $S = 2$. This state resembles a Laughlin state $\nu = 1/3$. (b)–(c) $V_0 = 1$, $B = 11$ T, and $S = 0$. This state resembles a $\nu = 2/3$ state with two vortices added. (d) $V_0 = 2$, $B = 8$ T, and $S = 2$. This state resembles a $\nu = 1$ Laughlin state with a giant vortex consisting of three off-particle vortices added at the center of the dot.

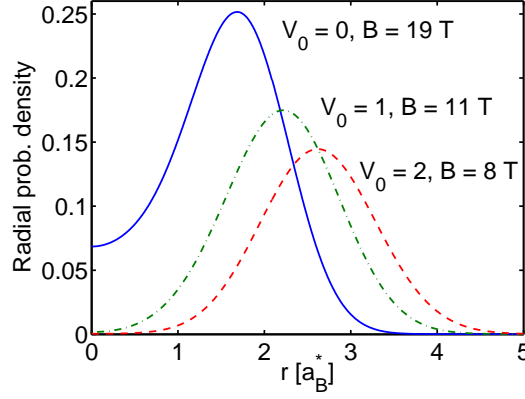


Figure 4.17: Radial probability density of the total angular momentum state $L = 18$. The confinement was the r^2 +Gaussian potential of Tab. 4.1. The magnetic fields for which the $L = 18$ state is a ground state are also marked in the plot.

a few spin states occurring in the phase diagram of Fig. 4.14. The vortex structure of the ground state given in Fig. 4.15 (a) is that of a $\nu = 1$ Laughlin state without off-particle vortices (compare with Eq. (2.71)). In Fig. 4.15 (b) and (c), the same angular momentum state is given after the spin transition $2 \rightarrow 0$. From the conditional wave function, it can be seen that the perturbation $V_0 = 2$ in the center of the dot has induced a vortex at the origin of the system. Assume that the Halperin wave function (2.72) can be extended like the Laughlin wave function in Eq. (2.71) with a prefactor that models off-particle vortices. Comparing the vortex structure with the Halperin wave function of Eq. 2.72, one finds that the structure is the same as that of a $\nu = 2$ integer QH state ("double-MDD" state) with one off-particle vortex.

In Fig. 4.16, the conditional wave functions of a ground state with angular momentum $L = 18$ are given for three different perturbation strengths V_0 . As seen from the phase diagram of Fig. 4.14, there is a 2-0-2 spin oscillation as a function of the perturbation strength in the state $L = 18$. The $V_0 = 0$ state in Fig. 4.16 (a) has a vortex structure close to that of a $\nu = 1/3$ Laughlin state. The test particle sees three vortices close to each of the other particles. Interestingly, the spin is zero when two off-particle vortices are added, and two when three central vortices are added. The state of Fig. 4.16 (b) and (c), with two off-particle vortices and $V_0 = 1$, has a vortex structure that agrees with a $\nu = 2/3$ Halperin state with a vortex prefactor. The state obtained

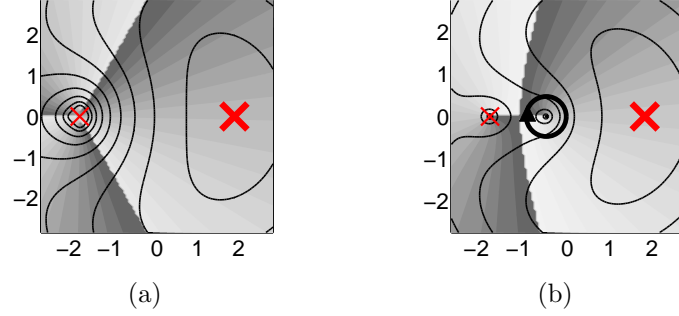


Figure 4.18: Conditional wave functions, as in Fig. 4.15, for the angular momentum state $L = 3$ of the r^2 +Gaussian system of Tab. 4.1. The two-electron system was calculated with and without perturbation: (a) $V_0 = 0$, $B = 15$ T, and $S = 1$. This is a $\nu = 1/3$ state. (b) $V_0 = 1$, $B = 8$ T, and $S = 1$. This is a $\nu = 1$ state with a single off-particle vortex at the center of mass. The structure of (b) was also found for the perturbation strength $V_0 = 2$.

with the perturbation $V_0 = 2$, given in Fig. 4.16 (d), has the same vortex structure as a $\nu = 1$ Laughlin state with three off-particle vortices. Here the central vortices do not completely coincide with each other at the center of mass. In Fig. 4.17, the radial probability densities of the three $L = 18$ states of Fig. 4.16 is plotted. As expected, the system becomes more ringlike and the electron density vanishes in a larger and larger region around the origin as the perturbation strength V_0 is increased.

In Fig. 4.18, the conditional wave function for a two-electron system with the r^2 +Gaussian potential of Tab. 4.1 is given. As the perturbation strength V_0 is increased, the $\nu = 1/3$ state changes to a $\nu = 1$ state with one off-particle vortex at the center of the dot. In contrast to the four-electron system, in the two-electron system there were found no spin transitions for constant total angular momenta.

Explanation of the spin oscillations

From the Laughlin wave function of Eq. (2.71) one finds that the total angular momentum of a spin polarized $\nu = 1/m$ state is determined by the formula

$$L_p = \frac{N(N-1)}{2}m + Nn_0, \quad (4.3)$$

where N is the number of electrons and n_0 the number of off-particle vortices. Similarly, using the Halperin wave function (2.72) with a off-particle vortex prefactor, like in the Laughlin wave function, one gets the total angular momentum of an unpolarized or a partially polarized state

$$L_u = \frac{N_\uparrow(N_\uparrow - 1)}{2}k + \frac{N_\downarrow(N_\downarrow - 1)}{2}k' + N_\uparrow N_\downarrow l + (N_\uparrow + N_\downarrow)n_0, \quad (4.4)$$

where N_\uparrow is the number of up spins, N_\downarrow is the number of down spins, k and k' give the total number of vortices seen by electrons with the same spin, and l is the total number of Pauli vortices seen by electrons with different spin. By symmetry, $k = k'$ when $N_\uparrow = N_\downarrow$ [34].

We are now going to explain the spin transitions at constant angular momenta seen in Fig. 4.14 using properties of the Halperin and Laughlin states. The Laughlin states can model only fully spin polarized states. The Halperin states can be used for unpolarized or partially polarized states. In a four-electron system there are three possible spin states: 0, 1, and 2. We therefore use the Halperin wave function to model spin 0 and 1 states, and the Laughlin wave function to model the spin 2 states.

In the special case of a system with four electrons, we get the angular momentum formulae

$$L_{u,0} = 2k + 4l + 4n_0, \quad L_{u,1} = 3k + 3l + 4n_0, \quad L_p = 6m + 4n_0, \quad (4.5)$$

where $L_{u,0}$, $L_{u,1}$ and L_p are the possible angular momenta of spin states 0, 1 and 2, respectively. Since m has to be an odd integer, it can change in steps $\Delta m = 2i$, where $i \in \{0, \pm 1, \pm 2, \dots\}$. This means that a four-electron system can change between different $\nu = 1/m$ states only by adding or removing $3i$ vortices.

Assume we start with the $\nu = 1$ state with angular momentum $L = 6$ in the four-electron case. Let the angular momentum be fixed. To be able to add a single vortex to the system, according to Eqs. (4.5) the new state must be another than a Laughlin state. Let us for a while assume that all the states can be described by either a Laughlin or Halperin wave function. As will be apparent later, this assumption does not generally hold, but it may, however, be a useful hypothesis. Using this assumption, the system must change either to the state $L_{u,0}$ or $L_{u,1}$. Consequently, the spin must change from 2 to 0 or 1. According to the expressions of Eqs. (4.5), if the angular momentum has to be kept constant, the spin 1 state is impossible, and the only possibility left is the spin 0 case, where $k = 1$ and $n_0 = 1$. That is exactly the kind of vortex and spin structure that was found after the first spin transition in the $L = 6$ state of the r^2 +Gaussian system (see Figs. 4.14 and 4.15 (b)–(c)):

The first excited $L = 6$ state has spin 0, one off-particle vortex and one Pauli vortex seen by particles with the same spin as the probe particle. If the only possible states are the Laughlin and Halperin states, according to the formulae of Eqs. (4.5) there does not exist any possible states with angular momentum $L = 6$ and more than one off-particle vortex. In fact, we did not find any other $L = 6$ states in the r^2 -Gaussian system.

Next, assume that we have the $\nu = 1/3$ state with angular momentum $L = 18$. The angular momentum is kept fixed, and also in this case we assume that the wave function must have a vortex structure similar to either the Halperin or Laughlin wave function. If one off-particle vortex is added, the only possibility is a spin 0 state. The (k, l) parameters can be either (1,3), (3,2) or (5,1). In our calculations, we did not find any state with only one off-particle vortex, but such a state might be present in a narrow interval of the perturbation V_0 . If two off-particle vortices are added, the only possibility according to Eq. (4.5) is a spin 0 state. There are two possibilities for the (k, l) parameters: (1,2) or (3,1). In our calculations we found the $L_{u,0}$ state with the parameters (1,2), i.e. a state with spin 0, two off-particle vortices, one Pauli vortex on the electron with the same spin and two Pauli vortices on the electrons with opposite spin. In the system with three off-particle vortices and total angular momentum 18, all spins 0, 1, and 2 are possible. The state with spin 2 must be a $\nu = 1$ Laughlin state with three off-particle vortices added. That is the state we found. According to Eq. (4.5), there should also be possible to have a spin 0 $L = 18$ state with four off-particle vortices added.

Let us define the integer m' such that $m = 2m' + 1$. Then, the angular momentum formula of spin polarized Laughlin states may be written

$$L_p = 6 + 12m' + 4n_0, \quad (4.6)$$

where m' and n_0 are non-negative integers. According to this expression, spin-polarized states can occur only at angular momenta $L_k = 6 + 4k$, where k is also a non-negative integer. This restriction of the occurrence of spin polarized states is in agreement with the results presented in the phase diagram of Fig. 4.14. Similarly, assuming that the state must be similar to either a Laughlin or Halperin state, according to the formulae (4.5) all odd angular momentum states should have spin 1. That is found to hold too, except for the cases of three angular momenta of the unperturbed parabolic dot (see Fig. 4.14). However, it must be emphasized that these spin 1 states do not have a vortex structure similar to that of a Halperin wave function for any of the calculated points.

Above we used the assumption that all states can be described by a wave function with a vortex structure similar to that by either a Laughlin

or Halperin state, possibly multiplied by a vortex prefactor. In fact, in the angular momentum range $6 \leq L \leq 20$ of the pure parabolic system, the only states with such vortex structures were the states with angular momenta $L = 6, 10, 16, 18$ and 19 . In the r^2 +Gaussian system with perturbation strength $V_0 = 1$, the corresponding states were $L = 6, 10, 14$ and 18 . Thus, generally the systems can not be described by either Laughlin or Halperin wave functions. However, for the angular momenta $L = 6, 10, 18, 22, 26, 30$ and 34 , thus most of the states where spin oscillations occurred, the vortex structure of all states could be described by either Laughlin or Halperin wave functions. Let the selection of state be further restricted by the rule that if by Eqs. (4.5) all spin states are possible, then the spin polarized case should be chosen. Applying this rule, the spin oscillations at the angular momenta $L = 6, 10, 18, 22, 26, 30$, and 34 are all predicted by Eqs. (4.5).

We see that most of the observed spin oscillations at constant angular momenta are in fact predicted by the Laughlin and Halperin wave functions, if the corresponding angular momentum states can be described approximately by the Laughlin and Halperin functions. It must be emphasized that we do not expect a priori the system to be described very exactly by the Laughlin and Halperin wave functions when the perturbation strength is large, but these models seem to give the right vortex structures and spin states at most of the angular momenta $L_k = 6 + 4k$, where k is a non-negative integer. Koskinen *et al.* [28] calculated overlaps between Laughlin/Halperin wave functions and ED results with the LLL approximation for a four-electron parabolic QD. For the filling factors $\nu = 1, 2/3, 2/5$ and $1/3$ they got the values 1, 0.636, 0.931 and 0.958, respectively. The spin depolarization observed at low angular momenta L_k for sufficiently narrow ring structures can now be explained as a necessary result of that one or more off-particle vortices are added at a given magnetic field. Similarly, the polarization of high L_k states can be explained by that more off-particle vortices are added as the system becomes more ringlike.

4.3.5 The coupled dot–ring system

In Fig. 4.19, we have presented a spin phase diagram of a four-electron coupled dot–ring system with the r^2 +shifted Gaussian confinement of Tab. 4.1. The ground states were calculated for magnetic fields in the range 0–14 T with the perturbation strengths $V_0 = 0, 1$ and 2 . At magnetic fields above the MDD region, we found an interesting transition from a 0-1-0-1 spin periodicity to the periodicity 1-2-1-2. This is a clear deviation from the patterns seen in the other systems considered in this Thesis. Here spin 2 states did not occur only at angular momenta $L_k = 6 + 4k$, where $k \geq 0$

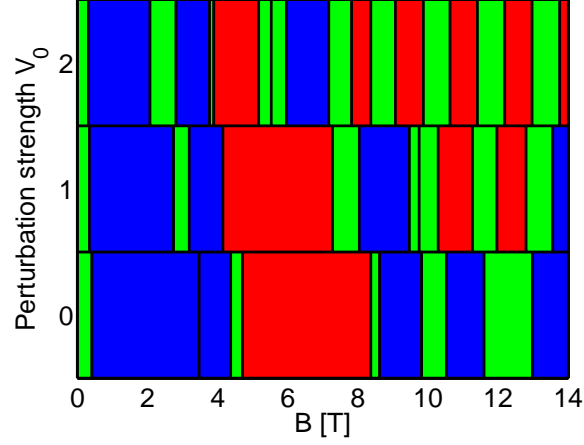


Figure 4.19: Spin state as a function of the magnetic field for a coupled dot–ring with the r^2 +shifted Gaussian potential of Tab. 4.1. The perturbation strengths V_0 are 0, 1 and 2, and the spin states are 0 (blue), 1 (green) and 2 (red).

is an integer, but at every second angular momentum value in the magnetic field region 8–14 T. As seen from Fig. 4.19, the applied shifted Gaussian perturbation is found to induce singlet–triplet transitions (spin transitions $0 \rightarrow 1$ and $1 \rightarrow 2$) at several different magnetic field values.

By studying radial charge densities and conditional wave functions, one can notice that two electrons were trapped in the central dot, whereas the two other electrons were located in the outer ring of the system (see Fig. 4.20). In the system with perturbation strength $V_0 = 2$, the two electrons trapped in the inner dot were found to have equal spins in the magnetic field range 8–14 T. This can be understood by that when the magnetic field increases, the angular momentum, and thus the kinetic energy, increases. Since the inner electrons are strongly trapped, the only way to lower the energy is to have equal spins, because then the Coulomb energy becomes lower due to the Pauli exclusion principle. The 1-2-1-2 periodicity seen in the system with perturbation strength $V_0 = 2$ can be understood by that only the outer electrons are allowed to change spin. In the system with perturbation strength $V_0 = 1$, the trapping of the inner electrons is less strict, and the inner electrons may therefore at some angular momenta flip the relative spin value.

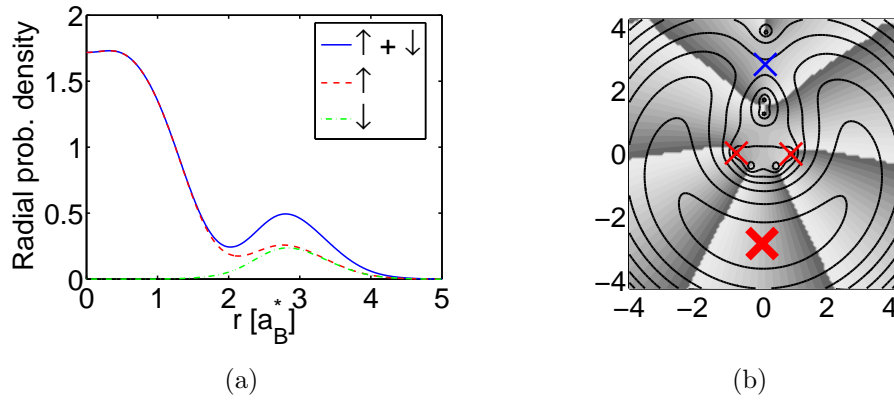


Figure 4.20: Left: Radial charge probability density of a coupled dot–ring with the r^2 +shifted Gaussian potential of Tab. 4.1. The state was $(L, S) = (13, 1)$, the magnetic field 9 T and the perturbation strength V_0 was 2. Right: Conditional wave function of the same system.

Chapter 5

Conclusions

In this Master's Thesis, we have studied different kinds of circularly symmetric quantum dots in a wide range of magnetic field values. As numerical tools, we have used the exact diagonalization and variational quantum Monte Carlo methods. In particular, we have studied spin effects and differences between different dot- and ringlike circular systems. The VMC calculations were done using single-configuration trial wave functions of the Slater-Jastrow type. Ground state energies and (L, S) ground states of the VMC and ED methods were compared with each other. We found that the VMC method with the used single-configuration trial wave functions gave energy values at most ca. 2 % higher than the values obtained in the ED calculations. For spin polarized states, the agreement was considerably better. The worst drawback with the single-configuration VMC method was that it failed almost completely to give the right spin ground states. All other calculations were therefore done using the ED method.

When comparing the spin structure of different circular systems, we found that states with high total angular momentum become spin polarized when the system becomes more ringlike, or alternatively approaches the circular hard-wall case. When the ring becomes sufficiently narrow, states with low angular momenta start to depolarize. The same trends were seen both in four- and six-electron systems, and the behaviour occurred similarly in two quite different sets of systems. We therefore suggest that this spin effect is only weakly dependent on the details of the confinement potentials. As long as the confinement potential is dot- or ringlike, the width of the (quasi)ring seems to be the most important parameter with respect to the spin structure.

To study systematically the transition between a parabolic and a ringlike system, we calculated the ground states for a parabolic dot with a Gaussian perturbation at the center of the dot. For different constant angular momenta, we found interesting oscillations between spin states as a function

of the perturbation strength. We showed that these spin oscillations could be predicted by the Laughlin and Halperin wave functions, when assuming that an increasing number of off-particle vortices are induced at the center of the dot when the perturbation becomes stronger. For constant perturbation strengths, we found 0-1-2-1 and 1-1-0-1 periodicities of the spin states as a function of the magnetic field. These spin sequences correspond to the ferromagnetic and antiferromagnetic Heisenberg models, respectively. The most important result of this study is the observation that the spin structure of different four-electron rings in many cases can be described either by the Heisenberg antiferromagnetic or ferromagnetic model. We observed phase transitions between ferromagnetic and antiferromagnetic regions as a function of the width of the ring and the magnetic field.

Our results indicate that tunable ring systems in a magnetic field may be modelled with a lattice Hamiltonian where the nearest-neighbour coupling constant of the Heisenberg term is a function of the magnetic field and the width of the ring. Because of a smaller Hilbert space, calculations with lattice Hamiltonians that contain the Heisenberg model may be more efficient than the continuum model for determining ground state properties of extended quantum ring systems. It should be possible to construct a parabolic dot with a tunable perturbation at the center of the dot, for example by using a metallic electrode with tunable voltage. As we found in our studies, this kind of system gives a very rich spin structure, which perhaps could be utilized in a spintronic device. The dynamics in transitions between different states can often be described by the Landau–Zener model, in which the probability for an adiabatic transition to another ground state depends exponentially on the transition velocity.

We also studied a parabolic dot with a ring-shaped perturbation. This coupled dot-ring system was found to have a clearly different spin behaviour than the dots and rings considered. When the perturbation was sufficiently strong, two of the four electrons became trapped in the central dot, both with equal spin. This gave a 1-2-1-2 spin periodicity as a function of the magnetic field, whereas the unperturbed system showed a 0-1-0-1 periodicity.

This work could be continued by, for example, developing proper tools for studying circular systems with a larger number of electrons. As we found, the results of the single-configuration VMC method are not satisfactory when studying spin effects. It would be interesting to try to find more suitable trial wave functions for different circular quantum dots, and possibly implement a quantum Monte Carlo diagonalization method [53] to get multi-configuration states. It should still be studied whether the spin structure of systems with other numbers of electrons can be described by the ferromagnetic and antiferromagnetic Heisenberg models, as we observed in the four-electron systems.

It would be interesting to model tunable quantum rings with some kind of lattice Hamiltonian where the nearest-neighbour coupling constant of the Heisenberg term is a function of the magnetic field and the width of the ring.

Bibliography

- [1] D. D. Awschalom and M. E. Flatté,
Challenges for semiconductor spintronics,
Nature Phys. **3**, 153 (2007).
- [2] S. Das Sarma,
Spintronics,
American Scientist **89**, 516 (2001).
- [3] I. Zutíć, J. Fabian, and S. Das Sarma,
Spintronics: Fundamentals and applications,
Rev. Mod. Phys. **76**, 323 (2004).
- [4] D. Loss and D. P. DiVincenzo,
Quantum computation with quantum dots,
Phys. Rev. A **57**, 120 (1998).
- [5] D. P. DiVincenzo, D. Bacon, J. Kempe, G. Burkard, and K. B. Whaley,
Universal quantum computation with the exchange interaction,
Nature **408**, 339 (2000).
- [6] Z. F. Ezawa,
Quantum Hall effects, Field theoretical approach and related topics,
World Scientific Publishing, Singapore (2008).
- [7] A. Khare,
Fractional statistics and quantum theory,
World Scientific Publishing, Singapore (1997).
- [8] R. E. Prange,
In *The quantum Hall effect*, ed. by R. E. Prange and S. M. Girvin,
Springer-Verlag, Berlin, p. 16–17 (1987).
- [9] R. B. Laughlin,
In *The quantum Hall effect*, ed. by R. E. Prange and S. M. Girvin,
Springer-Verlag, Berlin, p. 233 (1987).

-
- [10] S. M. Reimann and M. Manninen,
Electronic structure of quantum dots,
Rev. Mod. Phys. **74**, 1283 (2002).
- [11] J. K. Jain and T. Kawamura,
Composite fermions in quantum dots,
Europhys. Lett. **29**, 321 (1995).
- [12] R. B. Laughlin,
Anomalous quantum Hall effect: An incompressible quantum fluid with fractionally charged excitations,
Phys. Rev. Lett. **50**, 1395 (1983).
- [13] J. Kyriakidis, M. Pioro-Ladriere, M. Ciorga, A. S. Sacharajda, and P. Hawrylak,
Voltage-tunable singlet-triplet transition in lateral quantum dots,
Phys. Rev. B **66**, 035320-1 (2002).
- [14] T. Ihn, A. Fuhrer, K. Ensslin, W. Wegscheider, and M. Bichler,
Spin effects in a quantum ring,
Physica E **26**, 225 (2005).
- [15] A. Fuhrer, T. Ihn, K. Ensslin, W. Wegscheider, and M. Bichler,
Singlet-triplet transition tuned by asymmetric gate voltages in a quantum ring,
Phys. Rev. Lett. **91**, 206802-1 (2003).
- [16] A. K. Hüttel, K. Eberl, and S. Ludwig,
A widely tunable few electron droplet,
J. Phys.: Cond. Mat. **19**, 236202 (2007).
- [17] Y. Hancock, J. Suorsa, E. Tölö, and A. Harju,
Fractional periodicity and magnetism of extended quantum rings,
Phys. Rev. B **77**, 155103-1 (2008).
- [18] M. Koskinen, M. Manninen, B. Mottelson, and S. M. Reimann,
Rotational and vibrational spectra of quantum rings,
Phys. Rev. B **63**, 205323-1 (2001).
- [19] S. Elliott,
The physics and chemistry of solids,
John Wiley & Sons, Chichester (1998).

-
- [20] Web page of Nano-electronics group at the University of Basel,
<http://pages.unibas.ch/phys-meso/Pictures/pictures.html>
visited 14.10.08.
- [21] L. Jacak, P. Hawrylak, and A. Wójs,
Quantum dots,
Springer-Verlag, Berlin (1998).
- [22] C. Webb,
Edge tunnelling in quantum Hall systems,
Master's Thesis, Helsinki University of Technology (2008).
- [23] A. Harju,
Variational Monte Carlo for interacting electrons in quantum dots,
J. Low Temp. Phys. **140**, 181 (2005).
- [24] V. Fock,
Bemerkungen zur Quantelung des harmonischen Oszillators im Magnetfeld,
Z. Phys. **47**, 446 (1928).
- [25] C. Wittig,
The Landau-Zener formula,
J. Phys. Chem. B **109**, 8428 (2005).
- [26] M. Born and V. Fock,
Beweis des Adiabatensatzes,
Z. Phys. **51**, 165 (1928).
- [27] G. E. Murgida, D. A. Wisniacki, and P. I. Tamborenea,
Coherent control of interacting electrons in quantum dots via navigation in the energy spectrum,
Phys. Rev. Lett. **99**, 036806 (2007).
- [28] M. Koskinen, S. M. Reimann, J.-P. Nikkarila, and M. Manninen,
Spectral properties of rotating electrons in quantum dots and their relation to quantum Hall liquids,
J. Phys.: Condens. Matter **19**, 076211 (2007).
- [29] M. Manninen, M. Koskinen, S. M. Reimann, and B. Mottelson,
Magnetic properties of quantum dots and rings,
Eur. Phys. J. D **16**, 381 (2001).

-
- [30] S. Viefers, P. Koskinen, P. Singha Deo, and M. Manninen,
Quantum rings for beginners: energy spectra and persistent currents,
Physica E **21**, 1 (2004).
- [31] K. von Klitzing, G. Dorda, and M. Pepper,
New method for high-accuracy determination of the fine-structure constant based on quantized Hall resistance,
Phys. Rev. Lett. **45**, 494 (1980).
- [32] D. C. Tsui, H. L. Störmer, and A. C. Gossard,
Two-dimensional magnetotransport in the extreme quantum limit,
Phys. Rev. Lett. **48**, 1559 (1982).
- [33] H. L. Störmer,
The fractional quantum Hall effect,
Nobel lecture (1998).
- [34] T. Chakraborty and P. Pietiläinen,
The quantum Hall effects – Fractional and integral,
Springer-Verlag, Berlin (1995).
- [35] H. L. Störmer,
In *Advances in Solid State Physics*, ed. by P. Grosse,
Vol. 24, p.25, Vieweg, Braunschweig (1984).
- [36] R. B. Laughlin,
Quantized Hall conductivity in two dimensions,
Phys. Rev. B **23**, 5632 (1981).
- [37] J. K. Jain,
Composite-fermion approach for the fractional quantum Hall effect,
Phys. Rev. Lett. **63**, 199 (1989).
- [38] R. Jastrow,
Many-body problem with strong forces,
Phys. Rev. **98:5**, 1479 (1955).
- [39] A. H. MacDonald, S. R. E. Yang, and M. D. Johnson,
Quantum dots in strong magnetic fields: stability criteria for the maximum density droplet,
Austr. J. Phys. **46**, 345 (1993).
- [40] A. M. Tsvelik,
Quantum field theory in condensed matter physics,
Cambridge Univ. Pr., Cambridge, (2007).

-
- [41] D. R. Leadley *et al.*,
Fractional quantum Hall effect measurements at zero g factor,
Phys. Rev. Lett. **79** 4246 (1997).
- [42] G. Salis, Y. Kato, K. Ensslin, D. C. Driscoll, A. C. Gossard, and D. D. Awschalom,
Electrical control of spin coherence in semiconductor nanostructures,
Nature **414**, 619 (2001).
- [43] F. Schwabl,
Quantum mechanics, Third ed.,
Springer-Verlag, Berlin, (2002).
- [44] M. Kasner and W. Apel,
A new proposal for a quasi-electron trial wave function for the FQHE on a disk,
Europhys. Lett. **20**, 715 (1992).
- [45] J. K. Jain,
Incompressible quantum Hall states,
Phys. Rev. B **40**, 8079 (1989).
- [46] R. Morf and B. I. Halperin,
Monte Carlo evaluation of trial wave functions for the fractional quantized Hall effect: Disk geometry,
Phys. Rev. B **33**, 2221 (1986).
- [47] S. M. Girvin and A. H. MacDonald,
In *Perspectives in quantum Hall effects*, ed. by S. Das Sarma and A. Pinczuk,
John Wiley & Sons, Toronto, p. 165–167 (1997).
- [48] B. I. Halperin,
Theory of the quantized Hall conductance,
Helv. Phys. Acta **56**, 75 (1983).
- [49] J. H. Oaknin, L. Martín-Moreno, and C. Tejedor,
Skyrmions and edge-spin excitations in quantum Hall droplets,
Phys. Rev. B **54**, 16850 (1996).
- [50] J. M. Thijssen,
Computational Physics,
Cambridge University Press, Cambridge (1999).

-
- [51] P. Laininen,
Todennäköisyys ja sen tilastollinen soveltaminen,
Otatieto, Helsinki (1998).
- [52] N. Metropolis, A. W. Rosenbluth, M. N. Rosenbluth, A. H. Teller, and
E. Teller,
Equation of state calculations by fast computing machines,
J. Chem. Phys. **21**, 1087 (1953).
- [53] S. Siljamäki,
Wave function methods for quantum dots in magnetic field,
Ph. D. dissertation, Helsinki University of Technology (2003).
- [54] A. Harju, B. Barbiellini, S. Siljamäki, R. Nieminen, and G. Ortiz,
*Stochastic gradient approximation: An efficient method to optimize many-
body wave functions*,
Phys. Rev. Lett. **79**, 1173 (1997).
- [55] X. Lin, H. Zhang, and A. M. Rappe,
*Optimization of quantum Monte Carlo wave functions using analytical
energy derivatives*,
J. Chem. Phys. **112**, 2650 (2000).
- [56] A. Harju, V. A. Sverdlov, and R. M. Nieminen,
*Variational wave function for a quantum dot in a magnetic field: A quan-
tum Monte Carlo study*,
Europhys. Lett. **41**, 407 (1998).
- [57] H. F. Jones,
Groups, representations and physics,
Institute of Physics Publishing, London, p. 109–120 (1998).
- [58] F. Schwabl,
Advanced quantum mechanics,
Springer-Verlag, Berlin, (1999).
- [59] S. S. Gylfadóttir,
Fundamental properties of quantum rings,
Licentiate thesis, Helsinki University of Technology (2007).
- [60] L. N. Trefethen and D. Bau,
Numerical linear algebra,
Soc. for Ind. and App. Math., Philadelphia (1997).

-
- [61] E. Räsänen, M. J. Puska, and R. M. Nieminen,
Maximum-density-droplet formation in hard-wall quantum dots,
Physica E **22**, 490 (2004).
- [62] S. Siljamäki, A. Harju, R. M. Nieminen, V. A. Sverdlov, and P. Hyvönen,
Various spin-polarized states beyond the maximum-density droplet: A quantum Monte Carlo study,
Phys. Rev. B **65**, 121306-1 (2002).
- [63] Z. Barticevic, M. Pacheco, and A. Latgé,
Quantum rings under magnetic fields: Electronic and optical properties,
Phys. Rev. B **62**, 6963 (2000).
- [64] T. Chakraborty,
Nanosopic quantum rings: A new perspective,
Adv. in Solid State Phys. **43**, 79 (2003).
- [65] E. Räsänen,
Electronic properties of non-circular quantum dots,
Ph. D. dissertation, Helsinki University of Technology (2004).
- [66] H. Saarikoski, A. Harju, M. J. Puska, and R. M. Nieminen,
Vortex clusters in quantum dots,
Phys. Rev. Lett. **93**, 116802-1 (2004).
- [67] A. Harju, S. Siljamäki, and R. M. Nieminen,
Wave-function for quantum-dot ground states beyond the maximum-density droplet,
Phys. Rev. B **60**, 1807 (1998).
- [68] P. A. Maksym and T. Chakraborty,
Effect of electron-electron interactions on the magnetization of quantum dots,
Phys. Rev. B **45**, 1947 (1992).
- [69] M. Wagner, U. Merkt, and A. V. Chaplik,
Singlet-triplet oscillations in quantum dots,
Phys. Rev. B **45**, 1951 (1992).
- [70] E. Tölö,
Numerical calculation of configuration-interaction matrix elements,
Special Assignment, Helsinki University of Technology (2006).

-
- [71] G. B. Arfken,
Mathematical methods for physicists, Fourth ed.,
Academic Press, San Diego (1995).
- [72] E. W. Weisstein,
Jacobi-Anger expansion,
In MathWorld – A Wolfram web resource,
<http://mathworld.wolfram.com/Jacobi-AngerExpansion.html>
visited 02.02.09.

Appendix A

Interaction matrix elements

In Sec. 3.3 we presented the ED method, where the time-independent Schrödinger equation is transformed to a matrix equation of finite dimension. To calculate the Hamiltonian matrix elements $H_{nm} = T_{nm} + U_{nm}$, where T_{nm} is the single-particle part and U_{nm} is the two-particle part, pair-interaction matrix elements v_{ijkl} must be calculated. We are now going to show how the elements v_{ijkl} used in the ED studies of this Thesis have been calculated numerically. The method was proposed and implemented by Eero Töölö [70].

As stated in Sec. 3.3, the interaction matrix elements can be written

$$v_{ijkl} = \delta_{\sigma_i, \sigma_k} \delta_{\sigma_j, \sigma_l} \int d\mathbf{r} \int d\mathbf{r}' \varphi_i^*(\mathbf{r}) \varphi_j^*(\mathbf{r}') v(\mathbf{r}, \mathbf{r}') \varphi_k(\mathbf{r}) \varphi_l(\mathbf{r}'), \quad (\text{A.1})$$

where the functions φ_i are the single-particle basis functions and $v(\mathbf{r}, \mathbf{r}')$ is the two-particle operator in coordinate representation. In a system with Coulomb interaction, the integrals to calculate are of the form

$$I = \int d\mathbf{r} \int d\mathbf{r}' \varphi_i^*(\mathbf{r}) \varphi_j^*(\mathbf{r}') \frac{1}{|\mathbf{r} - \mathbf{r}'|} \varphi_k(\mathbf{r}) \varphi_l(\mathbf{r}'). \quad (\text{A.2})$$

In a circularly symmetric system the single-electron wave functions may be written [21]

$$\varphi_i(r, \theta) = \frac{1}{\sqrt{2\pi}} R_i(r) e^{i\theta l}, \quad (\text{A.3})$$

where r is the radial coordinate, θ is the angular coordinate, i denotes a configuration with given quantum numbers and l is the angular momentum of the state. The radial functions $f_i(r)$ are normalized according to

$$\int_0^\infty dr r R_i^2(r) = 1. \quad (\text{A.4})$$

Substituting single-particle wave functions of the form (A.3) into the integral I , we get

$$I = \frac{1}{(2\pi)^2} \int_0^\infty dr_1 \int_0^{2\pi} d\theta_1 e^{i(l_k - l_i)\theta_1} R_i(r_1) R_k(r_1) \\ \times \int_0^\infty dr_2 \int_0^{2\pi} d\theta_2 e^{i(l_i - l_j)\theta_2} R_j(r_2) R_l(r_2) \frac{1}{r_{12}}, \quad (\text{A.5})$$

where $r_{12} = |\mathbf{r}_1 - \mathbf{r}_2|$, and \mathbf{r}_i is the coordinate vector of particle i .

In our calculations we will need the following Lemma:

Lemma A.1. $\int_0^\infty dr \int_0^{2\pi} d\theta e^{-ikr \cos(\theta - \phi)} = \frac{2\pi}{k}$.

Proof. Let $J_n(x)$ be a Bessel function of the first kind [71] with the parameter $n \in \mathbb{Z}$. The Jacobi-Anger identity [72] states

$$e^{ix \cos(\theta)} = \sum_{n=-\infty}^{\infty} i^n J_n(x) e^{in\theta}. \quad (\text{A.6})$$

Let us substitute this identity into the left hand expression of the Lemma. We get

$$\begin{aligned} \int_0^\infty dr \int_0^{2\pi} d\theta e^{-ikr \cos(\theta - \phi)} &= \int_0^\infty dr \int_0^{2\pi} d\theta \sum_{n=-\infty}^{\infty} i^n J_n(-kr) e^{in(\theta - \phi)} \\ &= \sum_{n=-\infty}^{\infty} i^n e^{in\phi} \int_0^{2\pi} d\theta e^{in\theta} \int_0^\infty dr J_n(-kr) \\ &= \sum_{n=-\infty}^{\infty} i^n e^{in\phi} 2\pi \delta_{n,0} \int_0^\infty dr J_n(-kr) \\ &= 2\pi \int_0^\infty dr J_0(kr) \\ &= \frac{2\pi}{k}, \end{aligned} \quad (\text{A.7})$$

which completes the proof. The last equality follows from the normalization of Bessel functions $\int_0^\infty dr J_\alpha(r) = 1$ for all $\alpha \in \mathbb{R}$. \square

Let us define the two-dimensional Fourier transform of a function $f(\mathbf{r})$ as

$$\hat{f}(\mathbf{k}) = \int_{\mathbb{R}^2} d\mathbf{r} f(\mathbf{r}) e^{-i\mathbf{k} \cdot \mathbf{r}}, \quad (\text{A.8})$$

with the inverse transform

$$f(\mathbf{r}) = \frac{1}{(2\pi)^2} \int_{\mathbb{R}^2} d\mathbf{k} \hat{f}(\mathbf{k}) e^{i\mathbf{k} \cdot \mathbf{r}}. \quad (\text{A.9})$$

Using the Lemma, the inverse Fourier transform, and the relations $\mathbf{r} \hat{=} (r, \theta)$, $\mathbf{k} \hat{=} (k, \varphi)$, $\mathbf{r}_1 \hat{=} (r_1, \theta_1)$ and $\mathbf{r}_2 \hat{=} (r_2, \theta_2)$, where r , k , r_1 and r_2 are radial coordinates and θ , φ , θ_1 and θ_2 are angles, we may now write

$$\begin{aligned} \frac{1}{r_{12}} &= \frac{1}{(2\pi)^2} \int_{\mathbb{R}^2} d\mathbf{k} \left\{ \int_{\mathbb{R}^2} d\mathbf{r} \frac{e^{-i\mathbf{k} \cdot \mathbf{r}_{12}}}{r_{12}} \right\} e^{i\mathbf{k} \cdot \mathbf{r}_{12}} \\ &= \frac{1}{(2\pi)^2} \int_{\mathbb{R}^2} d\mathbf{k} \left\{ \int_0^\infty dr r \int_0^{2\pi} d\theta \frac{e^{-ikr \cos(\theta-\phi)}}{r} \right\} e^{i\mathbf{k} \cdot \mathbf{r}_{12}} \\ &= \frac{1}{(2\pi)^2} \int_0^\infty dk k \int_0^{2\pi} d\varphi \frac{2\pi}{k} e^{ik(r_1 \cos(\varphi-\theta_1) - r_2 \cos(\varphi-\theta_2))}. \quad (\text{A.10}) \end{aligned}$$

Substituting Eq. (A.10) into Eq. (A.5) and writing $\theta_1 = \theta + \varphi$ and $\theta_2 = \theta + \varphi$, after a few intermediate steps we get

$$\begin{aligned} I &= \frac{1}{(2\pi)^2} \delta_{l_k+l_l, l_i+l_j} \int_0^\infty dk \\ &\quad \times \int_0^\infty dr \int_0^{2\pi} d\varphi e^{ikr \cos(\varphi)} e^{i(l_k-l_i)\varphi} R_i(r) R_k(r) \\ &\quad \times \int_0^\infty dr \int_0^{2\pi} d\varphi e^{ikr \cos(\varphi)} e^{i(l_l-l_j)\varphi} R_l(r) R_j(r). \quad (\text{A.11}) \end{aligned}$$

From the Kronecker delta function of Eq. (A.11) we see that the total angular momentum is conserved in the two-particle Coulomb interaction. The Jacobi-Anger identity (A.6) gives the relations

$$\int_0^{2\pi} d\theta e^{ikr \cos(\theta)} e^{i(l_k-l_i)\theta} = 2\pi i^{l_k-l_i} J_{l_k-l_i}(kr) \quad (\text{A.12})$$

and

$$\int_0^{2\pi} d\theta e^{-ikr \cos(\theta)} e^{i(l_i-l_k)\theta} = 2\pi (-i)^{l_k-l_i} J_{l_k-l_i}(kr). \quad (\text{A.13})$$

Finally we use the relations (A.12) and (A.13) in the expression (A.11), and get I as a product of two Hankel transforms [71] of order $|l_i - l_k|$,

$$\begin{aligned} I &= \delta_{l_k+l_l, l_i+l_j} \int_0^\infty dk \\ &\quad \times \int_0^\infty dr J_{|l_i-l_k|}(kr) R_i(r) R_k(r) \\ &\quad \times \int_0^\infty dr J_{|l_i-l_k|}(kr) R_j(r) R_l(r). \quad (\text{A.14}) \end{aligned}$$

The integrals I were calculated numerically according to Eq. (A.14) using the Romberg integration method.